Particle Accelerators, 1994, Vol. 43(4), pp. 195–230
Reprints available directly from the publisher
Photocopying permitted by license only

ADIABATIC PARTICLE MOTION IN SPATIALLY-VARYING WAVE STRUCTURES

DAVID L. BRUHWILER[†] and JOHN R. CARY*

[†]*Grumman Corporate Research Center, 4 Independence Way, Princeton, NJ 08540-6620, USA*

**Department of Astrophysical, Planetary and Atmospheric Sciences and Department of Physics, University of Colorado, Boulder, CO 80309-0391, USA*

(Received 11 September 1992; in final form 1 October 1993)

Adiabatic theory is applied to the longitudinal dynamics of particles interacting with a large-amplitude wave packet for bounce time that is short compared with the transit time. This analysis differs from previous ones in that the Hamiltonian varies slowly with the coordinate rather than with the time. The resulting adiabatic invariant is not equal, even in lowest order, to the usual action. This analysis correctly predicts the basic features of the interaction observed in previous numerical studies. Furthermore, our model captures the essential elements of the longitudinal dynamics of slow-wave structures such as radio-frequency quadrupoles, free-electron lasers and plasma beat-wave accelerators.

KEY WORDS: Particle dynamics, radio-frequency quadrupoles, free-electron lasers, beat-wave acceleration, adiabatic invariance, separatrix crossing

1 INTRODUCTION

We treat analytically the dynamics of charged particles trapping and detrapping in a one-dimensional traveling wave with an amplitude that varies slowly in space. The maximum amplitude of the wave is allowed to be arbitrarily large. Our results are relevant to the trapping of ions in a radio-frequency quadrupole[1] (RFQ), the trapping and detrapping of electrons in a free-electron laser[2] (FEL) with an appropriately tapered wiggler magnet, and the electron dynamics in a plasma beat-wave accelerator[3,4] (PBWA). In particular, we explain how to correctly match an ion beam to an RFQ (neglecting transverse motion) so as to minimize growth of the longitudinal emittance during trapping.

Wave-particle interactions are central to many physical phenomena in both plasma and accelerator physics. Nearly resonant particles, i.e., those with velocity close to the phase velocity of the wave, interact strongly with the wave. The large energy exchange between a traveling wave and its associated resonant particles is important

to plasma turbulence theory and crucial for charged-particle acceleration in slow-wave structures such as those mentioned above.

When the wave parameters vary slowly in time, by which we mean that the time scale for variation is long compared with the characteristic bounce time of trapped particles, adiabatic theory can be applied to the particle motion. In this limit, there exists an approximate invariant of the motion known as the adiabatic invariant.[5] To lowest order, the adiabatic invariant is equal to the familiar action, $I \equiv (1/2\pi) \oint p_z dz$, with both time and the value of the Hamiltonian held fixed during the integration. The action is proportional to the phase space area enclosed by a trajectory [see, e.g., References 6, 7 and 8].

Expanding on previous work,[9,10] we consider the case of wave parameters that vary slowly in space rather than time. This is the case that occurs most frequently in accelerator physics applications. Here, the stipulation of slow variation imposes two requirements on the wave structure. First, the length scale over which the wave amplitude varies must be long compared with the wavelength; otherwise, there would be no well-defined potential troughs to trap particles. Second, the transit time of particles resonant with the wave must be long compared with the characteristic bounce time of trapped particles.

Because adiabatic theory assumes the slow variation is in the independent variable, we must reverse the roles of space and time, which is permissible in Hamiltonian theory. In the resulting system, the new coordinate is the rapidly varying phase, $\phi \equiv \omega t - kz$, while the new time is the original coordinate z. Adiabatic theory can then be applied directly to this system, so our analysis consists largely of finding the new conjugate momentum and the new Hamiltonian.

We show below that the adiabatic invariant is *not* simply the familiar action from time-varying systems. This result runs counter to the physical intuition firmly established in the plasma and accelerator physics communities. Furthermore, the particle dynamics is far richer for the case of spatial variation, including phenomena such as ponderomotive reflection and even resonant reflection.

We present in Section 2 of this paper the Hamiltonian model chosen for the application of our new analytic methods. The two dimensionless parameters relevant to our analysis are ε and α_0, where ε is the ratio of the wavelength to the characteristic length scale over which the wave parameters change, and α_0 (proportional to the wave amplitude) is the maximum potential energy of a particle in the wave divided by the average kinetic energy of a resonant particle. The two criteria for an adiabatic analysis can be expressed simply as the requirement that ε and $\varepsilon/\alpha_0^{1/2}$ both be small. We then show in Section 3 how to apply adiabatic theory to this model and calculate the adiabatic invariant.

We discuss in Section 4 how contour plots of the adiabatic invariant reveal the underlying structure of the particle dynamics. For example, such plots clearly show the range of initial particle velocities that lead to ponderomotive reflection. In addition, these plots show in detail how three distinct, dynamical topologies appear as the parameter α_0 is increased from zero. It is seen for each of these three cases that nearly-resonant particles are trapped in the wave and that upon detrapping they ultimately attain one of two distinct final velocities, depending upon their initial phase. It is

furthermore shown that, for $\alpha_0 > \alpha_{T2} \approx 0.636$, there exist particles with initial velocities well removed from the phase velocity of the wave (i.e. they are not "nearly resonant" in the usual sense) which nevertheless interact resonantly with the wave and are subsequently very strongly reflected.

The ideas and results of Section 4 are used in Section 5 to provide an analytic explanation of the numerical work of Fuchs, Krapchev, Ram, and Bers[11] (hereafter referred to as FKRB). FKRB studied a dynamical system very similar to ours, and found that quasilinear theory broke down in the limit that ε and $\varepsilon/\alpha_0^{1/2}$ were both small. This is just the parameter regime which we study here.

The adiabatic contour plots of Section 4 show that the regime of ponderomotively reflected particles grows with α_0 until $\alpha_0 = \alpha_{T2}$, at which point it saturates. In Section 6, we make a detailed comparison between ponderomotive theory and our adiabatic analysis. In particular, we show that our analysis agrees with ponderomotive theory in the limit of small α_0, and that the two methods differ only slightly as α_0 approaches the critical value α_{T2}. For larger values of α_0, the two analyses make sharply different predictions, and numerical results confirm the adiabatic analysis.

This paper is a more detailed presentation of previously published work.[9,10,12] In fact, other work[13] has recently generalized certain aspects of what we present here to the relativistic case, in order to properly treat electron dynamics in a plasma beat-wave accelerator[4] in the adiabatic limit. However, here we have gone into much more detail on the different topological cases which arise as the parameter α_0 is changed. In Section 7, we discuss the relevance of our work to accelerating devices such as RFQ's, FEL's and PWBA's.

Finally, our conclusions are presented in Section 8.

Before proceeding to Section 2, we wish to emphasize that we have restricted our analysis to zero order in the small parameter $\varepsilon/\alpha_0^{1/2}$. To first order, the particle dynamics involve phase-dependent kicks in the value of the adiabatic invariant whenever a phase-space trajectory crosses the separatrix. This occurs during the process of trapping, detrapping, and resonant reflection. Such details have been studied previously[10] and will be published in a future paper.[14] To lowest order, these stochastic phenomena can be ignored for a single wave-particle interaction.

2 HAMILTONIAN MODEL

The Hamiltonian governing the 1-D motion of a nonrelativistic charged particle in an electrostatic wavepacket is

$$\begin{aligned} H_{wp}(z, p_z, t) &= p_z^2/2m + e\Phi(z, t) \\ &= p_z^2/2m + eA(z/L)\cos(kz - \omega t)\,, \end{aligned} \tag{1}$$

where z is the spatial coordinate, p_z the momentum, t the time, m the particle mass, e the particle charge, k the wave number, ω the wave frequency, Φ the electrostatic

potential, and A the envelope function of the wavepacket. The amplitude is assumed to have the form $A(z/L) = A_0 f(z/L)$, where f is a function of unit peak and unit width, so that A_0 is the peak value of the potential and L is the characteristic length over which the wave amplitude changes. Our analysis is readily applied to other functional forms of the wave envelope.

We now introduce dimensionless variables in order to simplify the notation. Let $T = \omega t$, $q = kz$, $p = (k/m\omega)p_z$, and $H = (k^2/m\omega^2)H_{wp}$. Substituting these variables into Equation (1) yields

$$H(q,p,T) = \frac{1}{2}p^2 + \alpha(\varepsilon q)\cos(q - T), \tag{2}$$

where $\varepsilon \equiv 1/kL$ and $\alpha = \alpha_0 f(\varepsilon q)$, with $\alpha_0 \equiv (k^2 e/m\omega^2)A_0$. The number of wavelengths within the wave envelope is given by $1/\varepsilon$; this number is large for a wavepacket, so ε is small. Trapped particles oscillate characteristically at the bounce frequency, $\omega_0 \equiv k(eA_0/m)^{1/2} = \omega\alpha_0^{1/2}$. Thus the dimensionless amplitude is the square of the ratio of the particle bounce frequency to the wave frequency, $\alpha_0 = (\omega_0/\omega)^2$.

A snap shot of the potential energy for our model is shown in Figure 1a. The smooth curve is the envelope function $f(\varepsilon q)$, which for this plot we take to be a gaussian. The separatrices of the corresponding phase space at an instant in time are shown in Fig. 1b, with the lobes corresponding to the potential wells of Fig. 1a. As time advances, the sinusoidal wiggles within the envelope in Fig. 1a move to the right at the phase velocity, as do the separatrix lobes in Fig. 1b. Thus, the separatrix lobes grow to some maximum value and then shrink back to nothing as they move from left to right.

The phase-space trajectory of a nearly resonant particle would enter Fig. 1b from the left and trap in a growing lobe. This lobe would ferry the oscillating trajectory to the right side of the wave, where the trajectory would eventually detrap as the lobe shrank. The characteristic time required for a resonant particle to cross the wavepacket is $kL/\omega = 1/\omega\varepsilon$.

The number of bounce oscillations executed by a resonant particle as it crosses the wavepacket is given by the product of the bounce frequency and the time for crossing the wavepacket: $v \equiv \omega_0/\omega\varepsilon = \alpha_0^{1/2}/\varepsilon$. For small v, no bounce oscillations are executed by such a particle, and its trajectory to lowest order is a straight line. It was shown by FKRB that quasilinear theory works well in this limit.

Except for small $\mathbf{O}(\varepsilon)$ differences, the Hamiltonian [Eq. (2)] includes that studied by FKRB. However, we analyze the large-v regime, where resonant particles execute many bounce oscillations in crossing the wavepacket. FKRB studied this regime numerically, finding the particle dynamics differed dramatically from that of the small-v regime. Our analysis explains some of their numerical results.

3 ADIABATIC INVARIANCE THEORY

Adiabatic invariance theory is useful in the limit that resonant particles execute many bounce oscillations when crossing the wavepacket, because it allows one to average

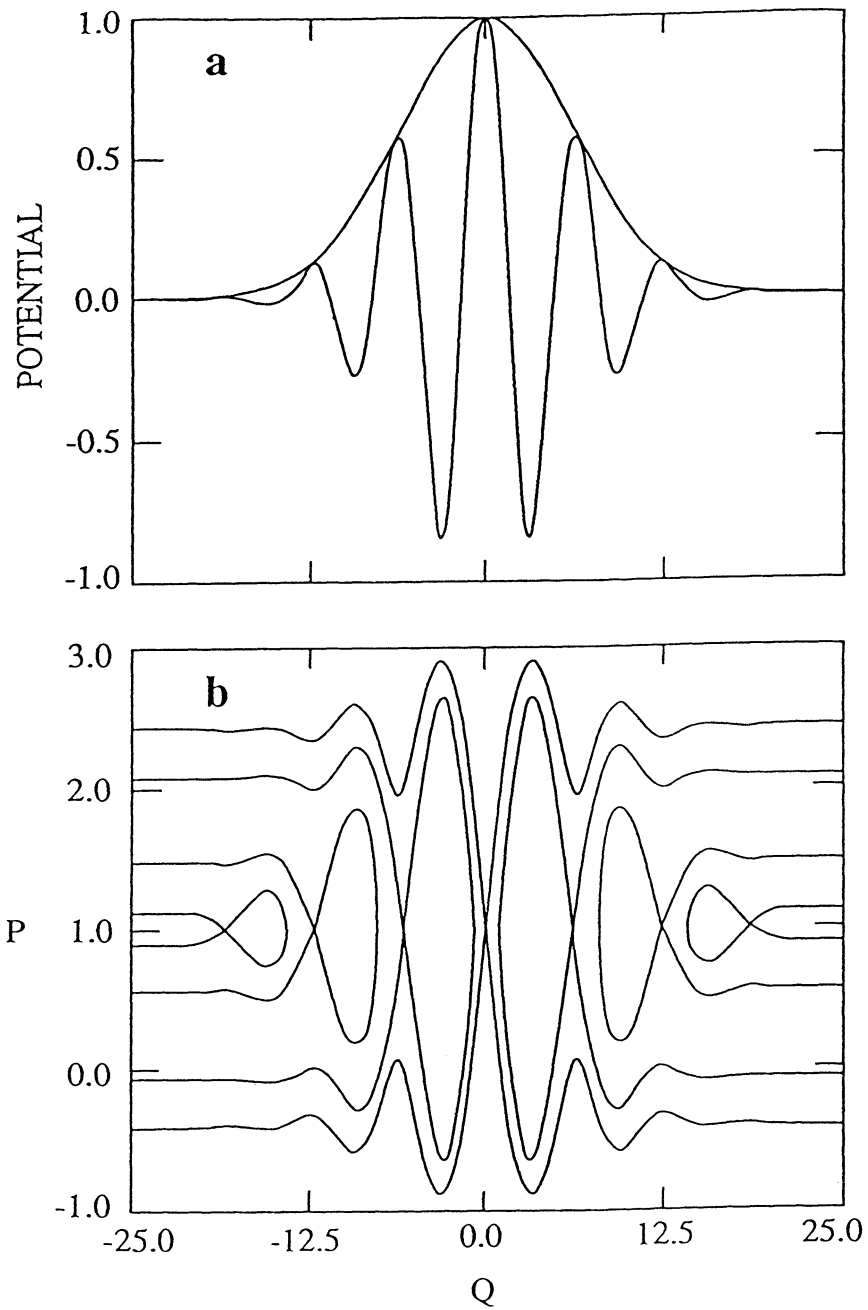

FIGURE 1: (a) The potential of the original Hamiltonian for $\alpha_0=1$ and $\varepsilon=0.12$. (b) The corresponding phase-space.

over these fast oscillations, thus simplifying the analysis. For adiabatic theory, the Hamiltonian must be a slow function of the independent variable, usually time. Our Hamiltonian has its slow variation in the spatial variable q, as is indicated formally by the dependence of the wave envelope on εq, where ε is small. Therefore, we first transform to a new Hamiltonian where q is treated as the independent variable, then we proceed to calculate the adiabatic invariant.

3.1 Preliminary Transformations of the Hamiltonian

We treat q as the independent variable simply by reversing the roles of the two conjugate pairs (q, p) and (T, H). The Hamiltonian, which we denote by the symbol E in order to emphasize its new role, becomes the new momentum and T its conjugate variable. Physically, E is the particle energy in the laboratory frame (i.e. the frame where the wave envelope is stationary). Likewise the momentum, which we now denote by P_1, serves as the Hamiltonian.

The functional form of this new Hamiltonian,

$$P_1(T, E, q) = \pm\sqrt{2[E - \alpha(\varepsilon q)\cos(T - q)]}\,, \tag{3}$$

is obtained by solving the equation $H(q, P_1, T) = E$ for P_1. This Hamiltonian has two branches: on the upper branch, where P takes the plus sign, the new time q increases along trajectories; on the lower branch, where P_1 takes the minus sign, q decreases along trajectories. As a result, phase space has two sheets — the upper sheet and the lower sheet — corresponding to these two branches.

In most laboratory applications the momentum will be everywhere positive, and only the upper branch of the Hamiltonian [Eq. (3)] will be used. However, the general case is treated here. We note that transformations of the above form are commonly used for Hamiltonian formulations of particle motion in accelerators [see, e.g., Ref. 15].

Again, adiabatic theory requires that the Hamiltonian vary slowly with the independent variable (here, q), while the Hamiltonian [Eq. (3)] has its q variation not only in the slowly varying amplitude $\alpha(\varepsilon q)$, but also in the rapidly varying phase $(T - q \equiv \phi)$. A canonical transformation, making the phase ϕ the new coordinate eliminates this fast variation in q. We achieve such a transformation with a generating function of the second kind,

$$F(T, K, q) = (T - q)K - \frac{1}{2}q\,, \tag{4}$$

which depends on the old coordinate T and the new momentum K.

The new coordinate is $\phi = \partial F/\partial K = T - q$, as desired. The momentum is actually unchanged by this transformation, as can be seen from the relation $E = \partial F/\partial T = K$. Therefore we keep our notation simple by dropping the symbol K and keeping E in its place. The second term on the right hand side of Equation (4) is used to simplify the physical interpretation of our new variables. The new Hamiltonian $P(\phi, E, \varepsilon q)$ is given by

$$P(\phi, E, \varepsilon q) = P_1[T(\phi, q), E, q] + \frac{\partial F}{\partial q}[T(\phi, q), E, q]$$
$$= -E \pm \sqrt{2[E - \alpha(\varepsilon q)\cos(\phi)]} - \frac{1}{2}. \tag{5a}$$

We now pause to interpret the physical meaning of our new Hamiltonian. Restoring physical units to Equation (5a) yields

$$\frac{\omega}{k}P = -E \pm \frac{\omega}{k}\sqrt{2m[E - eA(z/L)\cos(kz - \omega t)]} - \frac{1}{2}m\left(\frac{\omega}{k}\right)^2. \tag{5b}$$

The square root (including the $\pm$) is equal to p_z, the momentum in the lab frame. If we denote the phase velocity by v_ϕ, then we can write $P = -(E/v_\phi - p_z + mv_\phi/2) = -E_\phi/v_\phi$, where E_ϕ is the energy in the wave frame (i.e. the frame where the wave phase is stationary). We have defined E_ϕ in the usual way: $E_\phi \equiv p_\phi^2/2m + e\Phi$, where $p_\phi \equiv p_z - mv_\phi$ is the wave frame momentum.

We show the phase space of the Hamiltonian [Eq. (5a)] for $\alpha(\varepsilon q) = 2$ in Fig. 2. Specifically, Fig. 2 shows contours of constant $P(\phi, E, \varepsilon q)$, for a fixed value of εq, in the $E - \phi$ plane. One can imagine that the figure is wrapped around a vertical cylinder, so that $\phi = 0$ and $\phi = 2\pi$ are the same point. In Fig. 2, we have inverted the lower phase-space sheet and attached it to the bottom of the upper sheet.

We have patched the two phase-space sheets together in Fig. 2 in order to show the phase-space topology as clearly and simply as possible. However, this gives rise to a

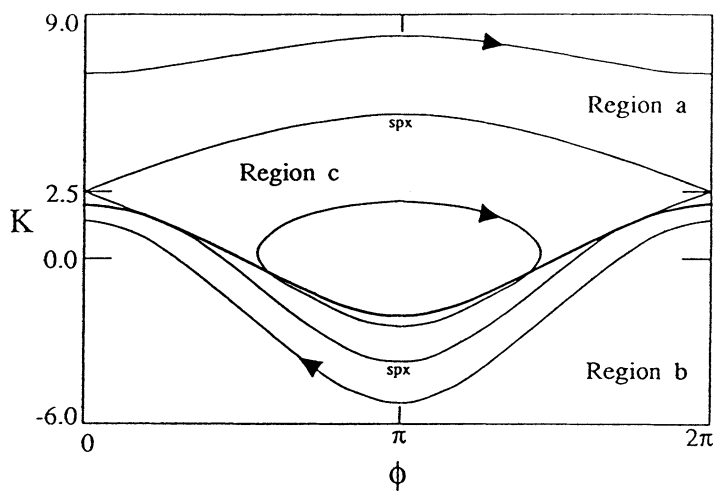

FIGURE 2: phase-space of the Hamiltonian in Eq. (5) for $\alpha(\varepsilon q)$=2. The thicker line corresponding to K=$\alpha(\varepsilon q)\cos\phi$ divides the two phase-space sheets. The two branches of the separatrix, labeled *spx*, divide the phase-space into three regions: region *a* above the separatrix, region *b* below the separatrix, and region *c* inside the separatrix.

slight complication, because a given value of E does not uniquely correspond to one phase space sheet or another. For this reason, we introduce a new variable K : $K = E$ on the upper sheet, while $K = 2\alpha(\varepsilon q)\cos(\phi) - E$ on the lower sheet. The thicker line in the figure, which corresponds to $K = E = \alpha(\varepsilon q)\cos(\phi)$, separates the two sheets.

In Fig. 2, the two branches of the separatrix are labeled *spx*. On these two curves, $E_\phi = -P = \alpha(\varepsilon q)$. Plugging $P = -\alpha$ in Eq. (5a) and solving for E yields the value of E on the separatrix:

$$E_{sx} = \alpha(\varepsilon q) + \frac{1}{2} \pm \sqrt{2\alpha(\varepsilon q)[1 - \cos(\phi)]}\,, \tag{6a}$$

where the + sign corresponds to the upper branch of the separatrix and the – sign corresponds to the lower branch. Given the above definition of our new variable K, we find that the value of K on the separatrix is $K_{sx} = E_{sx}$ on the upper phase space sheet. On the lower phase space sheet, where only the lower branch of the separatrix appears, we find

$$K_{sx} = \sqrt{2\alpha(\varepsilon q)[1 - \cos(\phi)]} + 2\alpha(\varepsilon q)\cos(\phi) - \alpha(\varepsilon q) - \frac{1}{2}\,, \tag{6b}$$

The separatrix divides the phase space into three regions. We call the region above the separatrix *region a*, and trajectories in this region are said to be *passing above*. In region a, $p > 1$ and $E_\phi = -P > \alpha(\varepsilon q)$. We call the region below the separatrix *region b*, and trajectories in this region are said to be *passing below*. In region b, $p < 1$ and $E_\phi > \alpha(\varepsilon q)$. We call the region inside the separatrix *region c*, where trajectories are trapped, and $E_\phi < \alpha(\varepsilon q)$. On the phase-space trajectories shown in regions a and b, $P = -4.2$. On the contour shown in region c, $P = 0.25$.

3.2 *Calculation of the Adiabatic Invariant*

Given a Hamiltonian that varies slowly with its independent variable, such as $P(\phi, E, \varepsilon q)$ with $\epsilon \ll 1$, there exists an adiabatic invariant[5] which can be written as a power series in ε. The lowest-order term in this series, denoted here by J, is the loop integral of the momentum around a phase-space trajectory:

$$J \equiv \frac{1}{2\pi}\oint d\phi E \equiv \frac{1}{2\pi}\oint d\phi(E_\phi + p_\phi + \frac{1}{2})\,. \tag{7}$$

The second equality follows from the definition of the wave-frame energy and momentum in dimensionless units. The third term in the parentheses simply adds a constant to the adiabatic invariant, so we will ignore it when calculating J below.

The value of the Hamiltonian P and the independent variable q (hence, the wave amplitude) are held fixed during the integration in Eq. (7). Because $E_\phi = -P$ [see the discussion below Eq. (6)], E_ϕ is held constant during the integration. Thus, the first term in the integral is $(E_\phi/2\pi)\oint d\phi$. This piece vanishes for trapped trajectories, which complete a full circuit in the phase, while it is just E_ϕ for passing trajectories, for which ϕ increases by 2_π in one period.

The second term in Eq. (7) gives the action integral familiar from the case of a wave with time-varying amplitude: $\bar{p}_\phi = (1/2\pi) \oint p_\phi d\phi$. This notation reflects our interpretation of $\bar{p}_\phi$ as an average momentum. For passing particles, $\bar{p}_\phi$ is in fact the average momentum on a phase-space contour of constant E_ϕ and fixed wave amplitude, and we choose the convention that it takes the sign of p_ϕ. For trapped particles, $\bar{p}_\phi$ is not precisely an average momentum, because the range of the trapped phase is not 2_π, and the integration is effectively of $|p_\phi|$ since $p_\phi d\phi$ remains positive when integrating around a circuit in phase. (Furthermore, we divide $\bar{p}_\phi$ by two for trapped particles so that it is continuous in magnitude as the separatrix is crossed.)

The adiabatic invariant for passing particles, J_P, and for trapped particles, J_T, has the form

$$J_P = \bar{p}_\phi + E_\phi \,; \tag{8a}$$

$$J_T = 2\bar{p}_\phi \,. \tag{8b}$$

Equation (8a) holds in phase-space regions a and b, while Eq. (8b) holds in region c. The adiabatic invariant for the case of time-varying wave amplitude can be recovered by removing the E_ϕ from Eq. (8a).

The average momentum $\bar{p}_\phi$ can be written as a function of E_ϕ and εq by explicitly evaluating the integral which defines it. By definition, $p_\phi = \pm[2E_\phi - 2\alpha(\varepsilon q)\cos\phi]^{1/2}$, which yields

$$\bar{p}_\phi(E_\phi, \varepsilon q) = \frac{2^{3/2}}{\pi}[E_\phi + \alpha(\varepsilon q)]^{1/2}\mathbf{E}(k)\,\mathrm{sign}(p_\phi) \qquad (\text{for } E_\phi > \alpha), \tag{9a}$$

$$= \frac{4}{\pi}\alpha^{1/2}(\varepsilon q)\left[\mathbf{E}(k^{-1}) + \frac{E_\phi - \alpha(\varepsilon q)}{2\alpha(\varepsilon q)}\mathbf{K}(k^{-1})\right] \quad (\text{for } E_\phi < \alpha), \tag{9b}$$

where $k(E_\phi, \varepsilon q) \equiv \{2\alpha(\varepsilon q)/[E_\phi + \alpha(\varepsilon q)]\}^{1/2}$, and the function *"sign"* returns the sign of its argument with unit magnitude, while $\mathbf{K}$ and $\mathbf{E}$ are complete elliptic integrals of the first and second kind, respectively.[16] These integrals have been obtained previously (Ref. 7 and p. 65 of Ref. 10). Equation (9a) holds for passing trajectories, while Eq. (9b) holds for trapped trajectories. For $p_\phi > 0$, the function $\bar{p}_\phi(E_\phi, \varepsilon q)$ is continuous and smooth for all values of E_ϕ and εq.

The adiabatic invariant is discontinuous across the separatrix, because it is defined by a different integral in each of the three regions of phase space. We define the *separatrix action* $Y(\varepsilon q)$ to be the value of J on the separatrix. Taking the limit $E_\phi \to \alpha$ of Eqs. (8) and (9), we obtain

$$Y_a(\varepsilon q) = \frac{4}{\pi}\alpha^{1/2}(\varepsilon q) + \alpha(\varepsilon q)\,, \tag{10a}$$

$$Y_b(\varepsilon q) = -\frac{4}{\pi}\alpha^{1/2}(\varepsilon q) + \alpha(\varepsilon q)\,, \tag{10b}$$

$$Y_c(\varepsilon q) = \frac{8}{\pi}\alpha^{1/2}(\varepsilon q)\,, \tag{10c}$$

with the subscripts on Y used to indicate the relevant region of phase space.

We now consider the form of the adiabatic invariant for passing particles far from the wave, where the local wave amplitude is vanishingly small. Taking the limit $\alpha \to 0$ of Eqs. (8a) and (9a) yields

$$j = \frac{1}{2}(p^2 - 1)\,, \tag{11}$$

where we have used a lower case j to indicate that this result holds only in the limit that the wave amplitude vanishes. Because momentum is conserved in this limit, it is reasonable that the adiabatic invariant should reduce to a simple function of the momentum.

4 UNDERLYING STRUCTURE OF THE DYNAMICS

In the adiabatic limit (i.e., in the limit $\varepsilon \ll 1$ and $\nu \gg 1$), trajectories remain on contours of the adiabatic invariant to lowest order in ε. Furthermore, this holds true even for trajectories that approach and encounter a separatrix.[17,18] Thus, a contour plot of the adiabatic invariant provides the underlying structure of the particle dynamics, without having to solve or numerically integrate the equations of motion.

4.1 Small-Amplitude Regime

We present such a contour plot in Fig. 3 for the case $\alpha_0 = 0.3$. The adiabatic invariant contours are plotted in the $\bar{p}_\phi - \varepsilon q$ plane. In order to generate such a plot, the E_ϕ in Eq. (8a) must be known as a function of $\bar{p}_\phi$ and εq. In fact, this function is known implicitly through the inversion of the function $\bar{p}_\phi(E_\phi, \varepsilon q)$ as given in Eq. (9a). The case $\alpha_0 = 0.3$ is in what we call the small-amplitude regime; the topology of the contours changes dramatically as the amplitude is increased beyond a critical value. This issue is discussed in detail below.

The two curves forming an outline of what resembles human lips are used to indicate the location of the upper and lower branches of the separatrix, where $E_\phi = \alpha(\varepsilon q)$. On these curves the average wave-frame momentum is $\bar{p}_\phi = \pm(4/\pi)\alpha^{1/2}(\varepsilon q)$. The contours above the lips correspond to trajectories in region a (passing above), those below the lips to trajectories in region b (passing below), and those inside the lips to trajectories in region c (trapped).

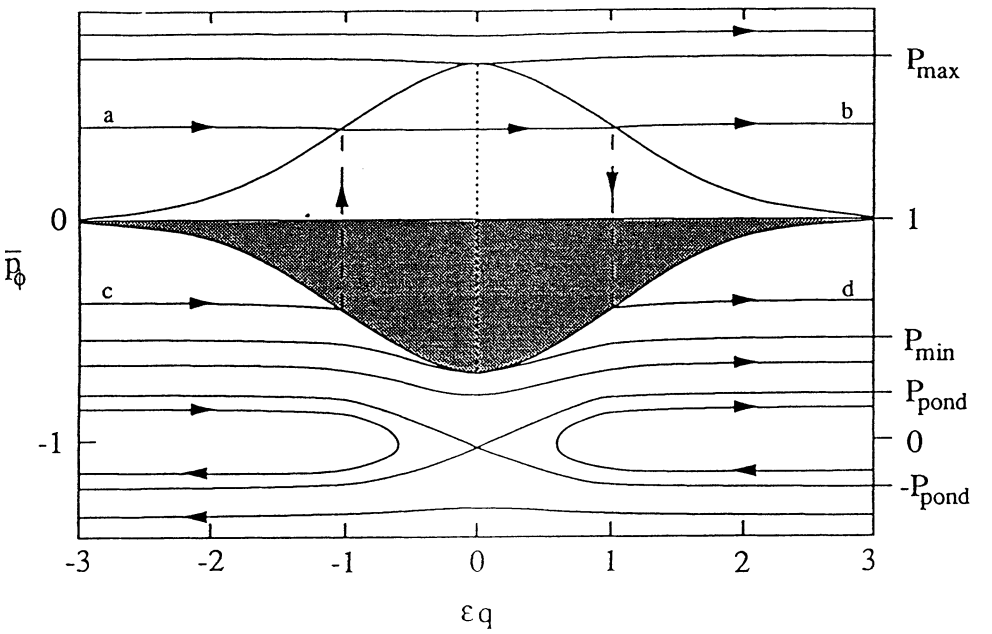

FIGURE 3: Action contours in the $\bar{p}_\phi - \varepsilon q$ plane, for $\alpha_0 = 0.3$, which is in the small-amplitude regime. The two curves which resemble lips indicate when the separatrix is crossed. That portion of the plot above the lips corresponds to particles that are passing above, while the upper half inside the lips corresponds to trapped particles, and that portion below the lips corresponds to particles passing below. The adiabatic invariant is undefined in the shaded area. The arrows indicate whether q is increasing or decreasing along the corresponding trajectories. The vertical dashed lines indicate possible transitions between two regions of phase-space upon crossing the separatrix. The contours which loop back on themselves correspond to ponderomotively reflected particles.

The arrows on the contours indicate the direction of particle motion. The direction on passing contours is determined at large distance, where the wave amplitude vanishes and $\bar{p}_\phi = p_\phi$. In this limit, the laboratory-frame momentum of each particle is given simply by $p = \bar{p}_\phi + 1$. Trapped particles move to the right (with the wave phase) at constant $\bar{p}_\phi$, which is proportional to the trapped-particle adiabatic invariant. The region inside the lower lip is shaded to indicate that it is unphysical: for trapped particles, $\bar{p}_\phi$ is positive by definition. The vertical dashed lines in Fig. 3 are used to connect contours in regions a and c with those in region b.

The underlying dynamical structure predicted by adiabatic theory has an unusual topology. Trajectories in a particular region of phase space make transitions to another region only by passing through the separatrix, which corresponds in our figure to the edges of the lips. At these points, transitions between any of the three regions are possible. This topology is obtained by cutting out the lower lip, folding the plane along the $\bar{p}_\phi$ axis, and connecting the plane along the edge of the upper lip, so that there are two distinct planes emanating upward from this lip. As we are restricted from using

pop-out figures, we must attempt to represent this topology in Fig. 3 with connecting lines.

We refer to those contours in Fig. 3 without arrows drawn on them as *critical contours*. The critical contours divide the plot into various sections in which the normal contours exhibit a common behavior. For example, the line which just grazes the upper lip (labeled on the right by $p_{\max}$) is a critical contour separating those contours in region a which do intersect the upper lip from those that do not. Trajectories which correspond to contours above this critical contour do not cross the separatrix. Grazing the bottom lip is a critical contour (labeled on the right by $p_{\min}$) separating those contours in region b which do intersect the lower lip from those that do not.

Various momentum values are listed on the right-hand side of Fig. 3. These values indicate the momentum of trajectories corresponding to these contours when they are far from the wave. In other words, the vertical axis on the right is obtained from the vertical axis on the left via the relation $p = \bar{p}_\phi + 1$, which holds in the limit $\alpha \to 0$.

To illustrate the interpretation of Fig. 3, we discuss the contours labeled a and c, both of which intersect the lips at the same wave amplitude. Upon encountering the separatrix, the two classes of corresponding trajectories combine into a single trapped class. The trapped trajectories then travel through the wave packet. Each trajectory detraps on the right side of the wave, corresponding then to either contour b or d, depending upon whether it is finally passing above or passing below.

Our analysis permits explicit calculation (to lowest order in ε) of the possible final values of momentum for a given value of incoming momentum. We illustrate this calculation for a trajectory corresponding to contour a. Far from the wave packet, a trajectory in phase-space region a has initial momentum p_i and, thus, adiabatic invariant $J_i = j(p_i) = (p_i^2 - 1)/2$ as given by Eq. (11). This value of the adiabatic invariant is conserved up to the separatrix, which is encountered when J equals the separatrix action, $Y_a = (4/\pi)\alpha^{1/2} + \alpha$ as given by Eq. (10a). The trapping amplitude α_x is obtained by equating J_i with Y_a, yielding

$$\alpha_x^{1/2}(p_i) = \frac{2}{\pi}\left(-1 + \sqrt{1 + \frac{\pi^2}{8}(p_i^2 - 1)}\right). \tag{12}$$

When the trajectory detraps, it is either passing above (i.e., corresponds to contour b) with final momentum $p_f = p_i$, or else it is passing below (i.e., corresponds to contour d). In the latter case, the adiabatic invariant changes to that of a trajectory on the separatrix in phase space region b: $J_f = Y_b(\alpha_x) = -(4/\pi)\alpha_x^{1/2} + \alpha_x$, as given in Eq. (10b). The trajectory then leaves the wave-packet region, preserving the adiabatic invariant, so that far from the wave its momentum satisfies $J_f = j(p_f) = (p_f^2 - 1)/2$. This chain of equalities gives the final momentum on contour d as a function of the initial momentum on contour a:

$$p_f = \sqrt{p_i^2 + \frac{32}{\pi^2}\left[1 - \sqrt{1 + \frac{\pi^2}{8}(p_i^2 - 1)}\right]}. \tag{13}$$

If we consider a trajectory initially corresponding to contour c, which traps in the wave and then, upon detrapping, is passing above (i.e., corresponds to contour b), then we can follow a procedure analogous to the one above and again obtain Eq. (13).

We define $p_{\max}$ to be the maximum value of p_i such that a trajectory will encounter the separatrix. Thus $p_{\max}$ can be found as a function of α_0 simply by noting that $\alpha_0 = \alpha_x(p_{\max})$ and then inverting Eq. (12) to obtain

$$p_{\max} \equiv \sqrt{1 + \frac{8}{\pi}\alpha_0^{1/2} + 2\alpha_0}\,. \tag{14a}$$

Likewise, we define $p_{\min}$ to be the minimum value of p_i such that a trajectory will encounter the separatrix. An analogous method then yields

$$p_{\min} \equiv \sqrt{1 - \frac{8}{\pi}\alpha_0^{1/2} + 2\alpha_0}\,. \tag{14b}$$

We emphasize that Eqs. (13) and (14) are independent of the explicit functional form of the wave envelope. Admittedly, we can obtain these analytic formulas only because we chose a relatively simple Hamiltonian to study. However, adiabatic invariant contour plots like Fig. 3 would still be useful (actually more so) when analytic formulae cannot be found, because information of this type could still be obtained graphically or numerically.

Towards the bottom of Fig. 3 is a critical contour containing an x-point, which we call the ponderomotive contour. The ponderomotive contour encloses all contours corresponding to ponderomotively-reflected trajectories, and two such reflected contours are shown. The upper part of the ponderomotive contour is labeled p_{pond}, while its lower part is labeled $-p_{\text{pond}}$. Those particles far to the left of the wave with $0 < p_i < p_{\text{pond}}$, as well as those particles far to the right of the wave with $-p_{\text{pond}} < p_i < 0$, will be ponderomotively reflected. These limits are symmetric about $p = 0$, because the limiting value of the adiabatic invariant $j(p)$ is symmetric about $p = 0$.

We explain in Appendix A how to find J_{pond}, the value of J on the ponderomotive contour. In general, this must be done numerically. Once J_{pond} is known, p_{pond} can be obtained by inverting Eq. (11), then letting $j \to J_{\text{pond}}$ and $p \to p_{\text{pond}}$:

$$p_{\text{pond}} \equiv \sqrt{2J_{\text{pond}} + 1}\,. \tag{15}$$

The value of J_{pond} depends only on α_0, not on the functional form of $\alpha(\varepsilon q)$.

4.2 *Intermediate-Amplitude Regime*

When α_0 exceeds the critical value $\alpha_{T1} \equiv 4/\pi^2$, the adiabatic invariant contours exhibit a new topology, which we refer to as the intermediate-amplitude regime. The reasons for this change in topology are best understood by considering the detailed particle dynamics in the vicinity of the separatrix;[10] however, such a discussion would be beyond the scope of this paper. Fortunately, somewhat simpler considerations, presented in Appendix B, are sufficient to determine the value of α_{T1}. The topology

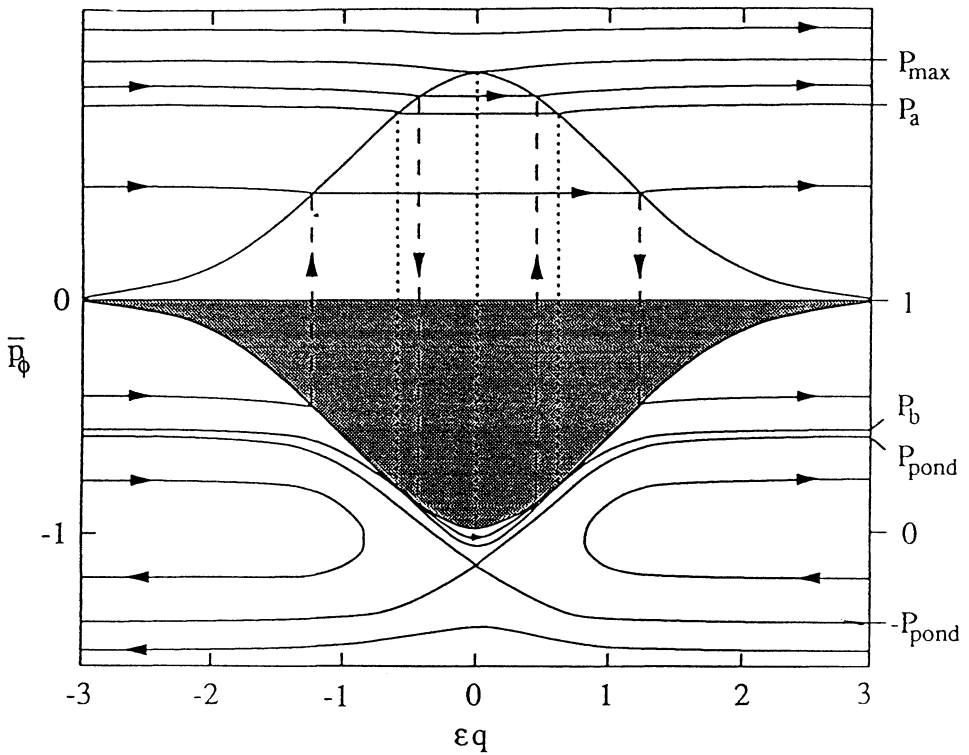

FIGURE 4: Action contours in the $\bar{p}_\phi - \varepsilon q$ plane for α_0=0.6, which is in the intermediate-amplitude regime.

of the intermediate-amplitude regime is shown in Fig. 4, where the maximum wave amplitude is $\alpha_0 = 0.6$. This topology is independent of the functional form of the wave envelope.

The critical contour in Fig. 4 labeled $p_{\max}$ is analogous to the one in Fig. 3, and $p_{\max}$ as a function of α_0 is given as before by Eq. (14a). Somewhat below, however, is a new critical contour, labeled p_a, which separates two types of contours in region a. Those contours below (familiar from Fig. 3) correspond to phase space trajectories which invariably trap in the wave, then detrap on the other side. Those above correspond to trajectories which, depending on their phase, either trap in the wave as before, or else scatter off the wave into phase space region b (following the short contour just below the lower lip), then encounter the separatrix again and scatter back into region a. For all such trajectories, p_f is equal in lowest order to p_i.

There is another new critical contour in Fig. 4, labeled p_b, which grazes the lower lip at the same two values of εq for which the p_a contour intersects the upper lip. This critical contour separates those contours in region b which correspond to separatrix-crossing trajectories from those which correspond to adiabatic trajectories, thus serv-

ing the same role as does the $p_{\min}$ contour in Fig. 3. The momenta p_a and p_b are found by using Eqs. (14a) and (14b), respectively, but with α_0 replaced by $\alpha_{T1} = 4/\pi^2$:

$$p_a = \sqrt{1 + 24/\pi^2}\,, \tag{16a}$$

$$p_b = \sqrt{1 - 8/\pi^2}\,. \tag{16b}$$

These results are valid for all $\alpha_0 \geq \alpha_{T1}$ and for any functional form of $\alpha(\varepsilon q)$.

The ponderomotive contour exists in the intermediate-amplitude regime as well, where we have again labeled the upper part p_{pond} and the lower part $-p_{\text{pond}}$. It is larger as shown in Fig. 4 than for the case shown in Fig. 3, and it has become distorted by the lower lip. The value of J on the ponderomotive contour, J_{pond}, must be found numerically, as is discussed in Appendix A. Once J_{pond} is known, p_{pond} can be obtained from Eq. (15).

4.3 Large-Amplitude Regime

As α_0 increases within the intermediate-amplitude regime, the critical contours labeled p_b and p_{pond} move closer together. We denote by α_{T2} the critical value of α_0 at which these two contours overlap and become one; α_{T2} marks the transition between the intermediate-amplitude and large-amplitude regimes.

The adiabatic invariant on critical contour p_b is, from Eqs. (11) and (16b), $J_P = -4/\pi^2$, while J_{pond} must be determined numerically. Thus the value of α_{T2} must be determined numerically by simultaneously finding E_ϕ and α_0 such that the two equations $\partial J_P/\partial \bar{p}_\phi = 0$ and $J_P = -4/\pi^2$ are both satisfied (see Appendix A). This is a root finding problem in two dimensions, and the value of α_0 obtained is by definition α_{T2}. We have obtained $\alpha_{T2} \approx 0.636$, which is accurate to three significant figures. This value is independent of the functional form of $\alpha(\lambda)$.

The new topology of the large-amplitude regime is shown in Fig. 5, where the maximum wave amplitude is $\alpha_0 = 2.5$. The critical contours labeled $p_{\max}$ and $p_{\min}$ are analogous to the ones in Fig. 3, with $p_{\max}$ given by Eq. (14a) and pmin given now by the negative of the quantity on the right hand side of Eq. (14b). Likewise, the critical contour p_a plays the same role as it did in Fig. 4 and the value of p_a is still given by Eq. (16a).

The ponderomotive contour in the large-amplitude regime is split into two separate contours by the lower lip. The one to the right of the lower lip is labeled p_{pond} at the upper end and $-p_{\text{pond}}$ at the lower end. In this regime, $p_{\text{pond}} = p_b$, which is still given by Eq. (16b). For all values of α_0 greater than α_{T2}, p_{pond} is equal to this fixed value. In other words, the range of initial momenta which result in ponderomotive reflection saturates once the large-amplitude regime is reached.

A new class of contours exists in the large-amplitude regime: those in region a that lie between the critical contours p_a and $p_{\max}$, as well as those in region b that lie between the ponderomotive contour and the critical contour $p_{\min}$. One such contour, labeled a, is shown in Fig. 5 intersecting the upper lip on the left side. Upon

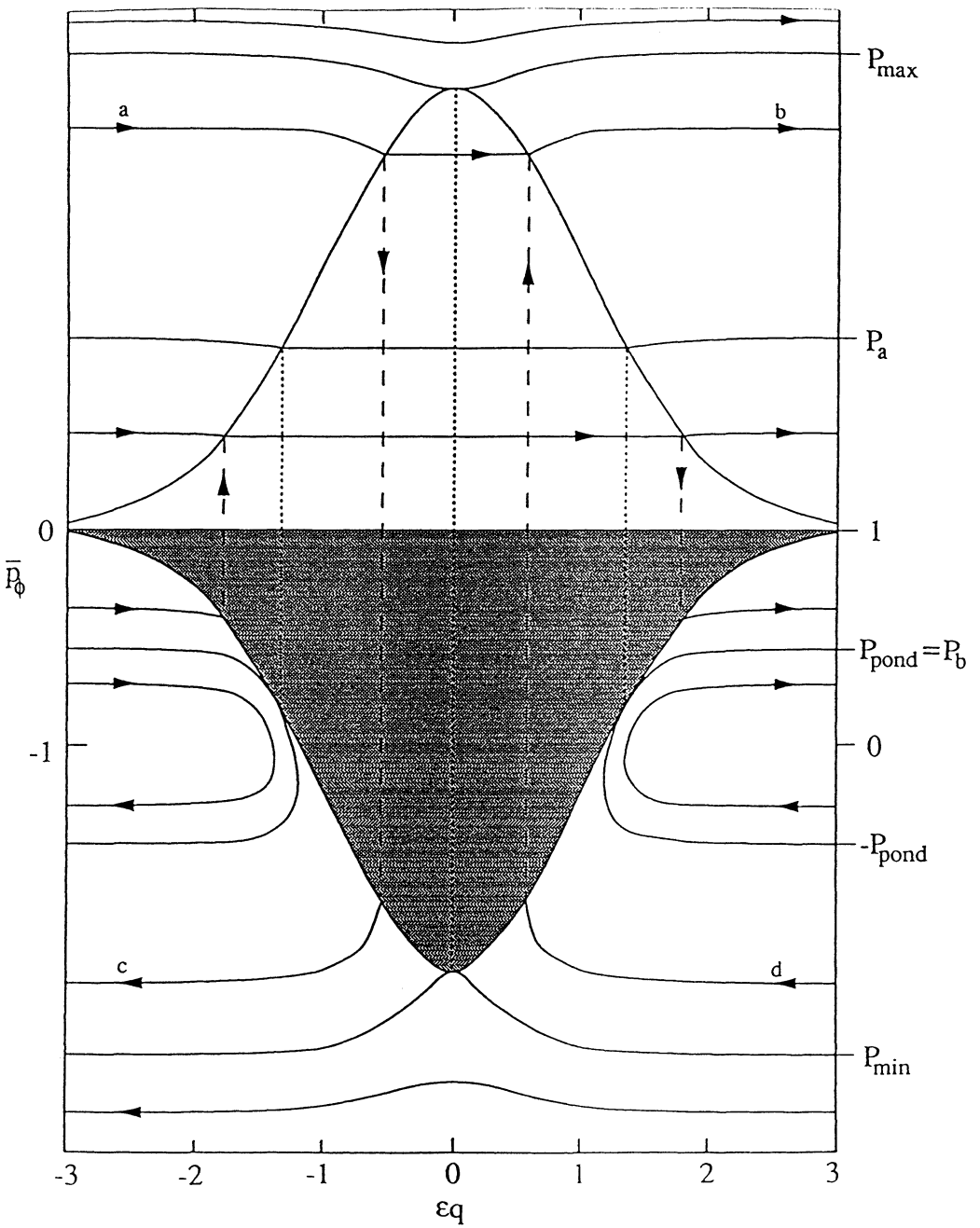

FIGURE 5: Action contours in the $\bar{p}_\phi - \varepsilon q$ plane for $\alpha_0=2.5$, which is in the large-amplitude regime.

encountering the separatrix, some of the corresponding trajectories (depending upon their phase) trap in the wave then detrap on the other side and finally correspond to the contour labeled *b*. For such trajectories, p_f is equal in lowest order to p_i.

However, there exist other trajectories corresponding to the initial contour *a* which can cross the separatrix from region *a* to region *b* (rather than becoming trapped) and thus are resonantly reflected by the wave, finally corresponding to the contour labeled *c*. For these trajectories, we can find p_f as a function of p_i just as we did in obtaining Eq. (13):

$$p_f = -\sqrt{p_i^2 + \frac{32}{\pi^2}\left[1 - \sqrt{1 + \frac{\pi^2}{8}(p_i^2 - 1)}\right]}, \tag{17a}$$

which is just Eq. (13) with a minus sign. To the right of the lower lip, we show another contour in this new regime, labeled *d*. All of the trajectories corresponding to this contour, regardless of phase, are resonantly reflected by the wave and finally correspond to contour *b*. For such trajectories, p_f is given in lowest order by

$$p_f = \sqrt{p_i^2 + \frac{32}{\pi^2}\left[1 + \sqrt{1 + \frac{\pi^2}{8}(p_i^2 - 1)}\right]}. \tag{17b}$$

Actually, the topology of the action contours in the large-amplitude regime is slightly more complicated than what we have presented in Fig. 5. As is explained in Appendix C, however, the differences affect only an exponentially-small class of trajectories. We do not show these details in Fig. 5 for the sake of clarity.

5 THE SKELETON OF A SCATTER PLOT

Here we provide a striking example of how the adiabatic-invariant contour plots are useful for understanding particle dynamics by using the same ideas to explain the scatter plot shown in Fig. 16b of FKRB, which is reproduced here in Fig. 6a in a slightly modified form. This figure, which somewhat resembles a flying bird, shows the results of a numerical simulation in which 5×10^3 particles, initially far from the wave and distributed uniformly in p_i between –2 and 4, interact once with a gaussian wave packet for which $\alpha_0 = 2$ and $\varepsilon = 0.1$. The final momentum of each particle, p_f, is plotted vs. p_i.

We present in Fig. 6b the same scattering plot for our model Hamiltonian, with $\alpha_0 = 2$ and $\varepsilon \to 0$. In other words, we plot p_f as a function of p_i according to the lowest-order dynamics predicted by adiabatic invariance theory. Our results accurately provide the skeleton of the "bird", even for ε as large as 0.1. The spread around this skeleton is due to phase-dependent separatrix-crossing effects. (Such effects are beyond the scope of this paper; they have been studied in detail elsewhere.)[10,17,18] When there is no interaction with the separatrix, the skeleton is precise.

Figure 6b was obtained from Fig. 5 and the results of the previous section as follows. For $p_i < p_{\min}$, all trajectories remain adiabatic and so $p_f = p_i$, which yields

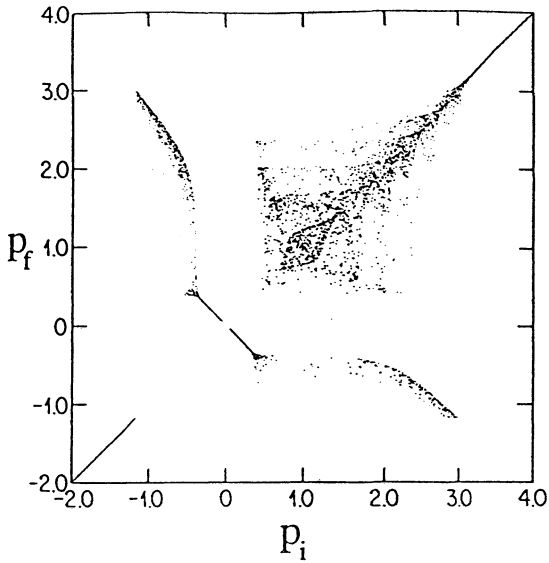

FIGURE 6a:

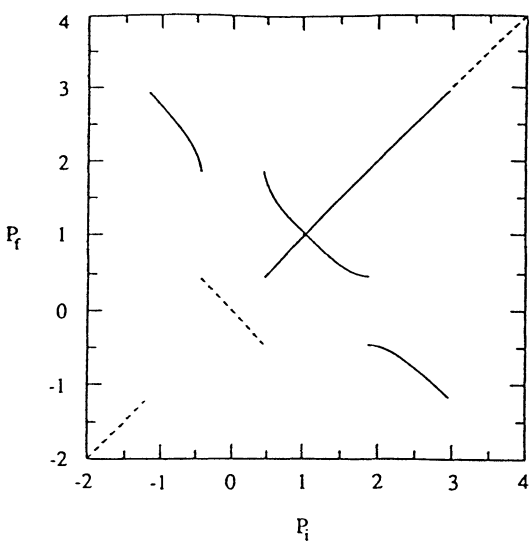

FIGURE 6b:

FIGURE 6: (a) Numerical results adapted from Ref. 11 for the final momentum as a function of the initial momentum, with $\alpha_0=2$ and $\varepsilon=0.1$. (b) The value of p_f after one wave-particle interaction as a function of p_i, for $\alpha_0=2$ and $\varepsilon\to 0$. Dashed lines are used to indicate that the interaction was adiabatic, including the one with negative slope, which corresponds to ponderomotive reflection. The solid lines indicate that the interaction was resonant, which means that the separatrix was crossed.

the straight dashed-line segment with unit slope in the lower left-hand corner. For $p_{\min} < p_i < -p_{\text{pond}}$, all trajectories are resonantly reflected by the wavepacket and p_f is given by Eq. (17b), which yields the curved line in the upper left-hand corner (i.e., the left wing of the bird). For $-p_{\text{pond}} < p_i < p_{\text{pond}}$, all trajectories are ponderomotively reflected so that $p_f = -p_i$, which yields the straight dashed line segment with a slope of negative unity. For $p_{\text{pond}} < p_i < p_a$, all trajectories trap in the wave and then detrap either with $p_f = p_i$ or with p_f given by Eq. (13) depending on their initial phase, yielding the lower part of the long straight-line segment with unit slope, as well as the intersecting curved line with negative slope. For $p_a < p_i < p_{\max}$, depending on their initial phase, trajectories either trap in the wave and subsequently detrap with $p_f = p_i$, or else they are resonantly reflected by the wave with p_f given by Eq. (17a), which yields the upper part of the long straight-line segment with unit slope, and the curved line in the lower right-hand corner (the right wing of the bird), respectively. For $p_{\max} < p_i$, all trajectories remain adiabatic and so $p_f = p_i$, which yields the straight dashed line segment with unit slope in the upper right-hand corner. For $\alpha_0 = 2$, we find that $p_{\min} \approx -1.18$, $p_b = p_{\text{pond}} \approx 0.435$, $p_a \approx 1.85$, and $p_{\max} \approx 2.93$.

If we were to replot the skeleton in Fig. 6b for smaller and smaller values of α_0, we would see both wings decrease in length as the range of initial momenta resulting in resonant reflection decreased. Simultaneously the solid line in the upper right would decrease in length and the dashed line in the lower left would extend towards the middle of the plot, as the regime of purely adiabatic motion increased. At the point where α_0 became equal to α_{T2}, the wings would have disappeared completely. Further decreases in α_0 would cause the figure to shrink further. In particular, the dashed line with negative slope would begin to reduce in length as the regime of ponderomotive reflection shrank. This process would continue until, when α_0 were zero, the plot would consist of a single, continuous dashed line.

6 PONDEROMOTIVE REFLECTION

Now we discuss the issue of ponderomotive reflection in more detail. A ponderomotive Hamiltonian can be derived by transforming away rapid small-amplitude oscillations of the trajectories (see Eq. (59) of Ref. 19). If we assume the electric field is longitudinal, ignore the transverse degrees of freedom, and take the nonrelativistic limit, then, in our dimensionless variables, the ponderomotive Hamiltonian is

$$H_{\text{pond}}(q,p) = \frac{1}{2}p^2 + \frac{1}{4}\alpha^2(\varepsilon q)(1-p^2)^{-1} = E_{\text{pond}}\,. \tag{18}$$

The ponderomotive calculation requires a small-amplitude expansion, so α^3 and higher-order terms have been neglected in obtaining Eq. (18). We have also neglected terms that are smaller than α^2 by $\mathbf{O}(\varepsilon)$.

The ponderomotive Hamiltonian is conserved to the extent that the ponderomotive approximation holds, so the associated phase space trajectories are just contours of constant H_{pond}. The H_{pond} contour which delimits the phase space region where ponderomotive reflection occurs must contain an x-point. This x-point occurs at

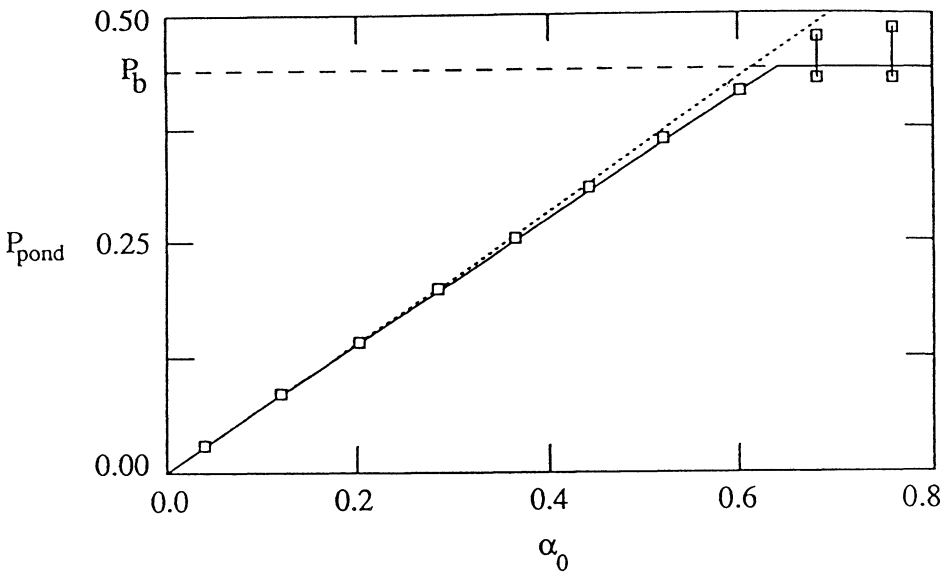

FIGURE 7: The value of $p_{\rm pond}$ is shown as a function of the maximum wave amplitude α_0. The solid line comes from adiabatic invariance theory; it saturates at $p_{\rm pond}=p_b$, which is indicated by the horizontal dashed line. The dotted line shows $p_{\rm pond}$ as given by standard ponderomotive theory; the line is straight with a slope of $2^{-1/2}$. The squares indicate values of $p_{\rm pond}$ obtained from numerical simulations.

$q = 0, p = \mathbf{O}(\alpha^2)$ where both partial derivatives of $H_{\rm pond}$ vanish. At the x-point (and, hence, on the contour containing it), $E_{\rm pond} = (1/4)\alpha_0^2[1+\mathbf{O}(\alpha_0)]$. Far from the wave, however, $E_{\rm pond} = (1/2)p_{\rm pond}^2$. Combining these two equations yields

$$p_{\rm pond} = 2^{-1/2}\alpha_0[1 + \mathbf{O}(\alpha_0)]\,. \tag{19}$$

We have obtained the same result analytically from adiabatic theory in the limit $\alpha_0 \ll 1$ (see Appendix D).

We show a plot of $p_{\rm pond}$ vs. α_0 in Fig. 7, comparing adiabatic theory, ponderomotive theory and numerical simulations. The solid line was obtained numerically from adiabatic theory, as described in Appendix A. It shows the saturation of $p_{\rm pond}$ at p_b (indicated by the horizontal dashed line) for $\alpha_{\geq}\alpha_{T2} \approx 0.636$. The dotted line was obtained from Eq. (19). The squares were obtained by numerically integrating the original equations of motion for $\varepsilon = 0.04$ and determining explicitly which initial conditions resulted in ponderomotive reflection and which did not.

For $\alpha_0 < \alpha_{T2}$ and $\varepsilon = 0.04$, the numerical simulations showed a definite value of $p_{\rm pond}$, such that ponderomotive reflection occurred with $p_i < p_{\rm pond}$ but not for $p_i > p_{\rm pond}$. Repeating the simulations with different initial phases indicated the size of the error bars, which were smaller than the size of the squares used to plot the points in Fig. 7.

For $\alpha_0 > \alpha_{T2}$ and $\varepsilon = 0.04$, and with p_i close to the value of p_{pond} given by adiabatic theory, all particles with p_i less than a certain value (which in turn was less than p_{pond}) were ponderomotively reflected, and all particles with p_i greater than a certain value (which in turn was greater than p_{pond}) crossed the separatrix. For p_i in between these two limiting values, particles either crossed the separatrix or were ponderomotively reflected, depending on their initial phase. The two squares connected by a line are used to show the two limiting values of p_i.

These nonadiabatic effects occur for $\alpha_0 > \alpha_{T2}$, because in that case all trajectories with p_i close to p_{pond} either cross the separatrix or else come very close to it. Therefore, the value of J can change by $\mathbf{O}(\varepsilon)$ and a given trajectory can be kicked across the critical contour. As ε is decreased, the two limiting values of p_i converge on $p_{\text{pond}} = p_b$, so in this limit the horizontal solid line represents a true division between initial momenta that result in ponderomotive reflection and those that do not.

The approximate agreement between the solid line and the squares in Fig. 7 indicates that adiabatic theory correctly predicts the value of p_{pond} for arbitrary values of α_0, in the limit of small ε. The close agreement between the solid line and the dotted line for $\alpha_0 \lesssim 0.2$ shows that adiabatic theory agrees with ponderomotive theory in the limit of small wave amplitude, as indeed it must. In addition, we note how closely ponderomotive theory agrees with adiabatic theory right up to the point of saturation, where $\alpha_0 = \alpha_{T2}$.

7 BEAM DYNAMICS IN ACCELERATING DEVICES

The Hamiltonian of Eq. (1) provides a simple model for the longitudinal beam dynamics of ions in an RFQ, and of electrons in a Compton-regime FEL or a plasma beat-wave accelerator (PBWA). We now briefly consider each of these accelerating devices.

7.1 Longitudinal Matching of an Ion Beam to an RFQ

The concept of an RFQ, which uses electric fields to both bunch and accelerate a beam of low-energy ions, was introduced by Kapchinskii and Teplyakov[1] in 1970. Ignoring both transverse degrees of freedom, the quadrupolar component of the longitudinal electrostatic potential is given by

$$\Phi(z,t) = -\frac{1}{2}V_0 F(z)\sin\left(\int k(z)dz\right)\cos(\omega t - \phi_0)\,, \tag{20a}$$

where z is the distance along the axis of the device, t is the time, V_0 is the voltage applied to the quadrupole vanes, $k(z)$ is the wave number, ω is the frequency, and ϕ_0 is a phase. The function $F(z)$ is given by

$$F(z) = \frac{m(z) - 1}{[m(z)]^2 I_0(ka) + I_0[m(z)ka]}\,, \tag{20b}$$

where I_0 is the zero-order modified Bessel function,[20] and the quantities a and $m(z)a$ are, respectively, the minimum and maximum distances between the quadrupole vanes and the axis of the device. Equations (20a) and (20b) are exact (for the longitudinal motion) if the vane surfaces satisfy Eq. (10) of Ref. 1.

We now consider a specific device, the 2.0-MeV RFQ[21] built at Los Alamos National Laboratory. This machine was used to accelerate negative hydrogen ions (H^-) up to energies of 2 MeV, with $\omega = 425$ MHz, $V_0 = 111.34$ kV, and with $a = 0.27$ cm and $m = 1.83$ at the end of the device. The wave number k is given locally by π/l_c, where l_c is the length of one of the unit cells of which the quadrupole vanes are constructed.[22] With 356 cells in a total length of 289.23 cm, an average value of k for this device is $k \approx 3.87\ \text{cm}^{-1}$.

Given these parameters, plus the mass and charge of the H^- ion and tabulated values of the modified Bessel function,[20] the maximum value of the dimensionless amplitude in our model would be

$$\alpha_0 = \frac{k^2 e V_0}{2m\omega^2} F_{\max} \approx 1.6\,, \tag{21}$$

which is in the large-amplitude regime. As can be seen from Eqs. (20a) and (20b), the functional form of $\alpha(\varepsilon q)$ would be quite complicated; however, many of the dynamical results obtained from the adiabatic-invariant contour plots are entirely independent of the wave amplitude's functional form.

It is slightly more problematic to determine the value of the small parameter ε for a real machine. In general, ε will be a local quantity which depends on the length scale over which system parameters are changing as compared with the length of a unit cell. For example, if one or more of the parameters changes by order unity over some distance L in one part of the machine, then the local value of ε will be $1/kL$, where k is the local value of the wave number. The trapping (and subsequent acceleration) of ions in an RFQ is done adiabatically in order to avoid losing particles.

Given that the Hamiltonian in Eq. (1) models the longitudinal dynamics of nonrelativistic ions trapping in an RFQ, we now use the results of Section 4 to show how to match an incoming beam (with some given momentum spread) to an RFQ in such a way that the longitudinal emittance of the trapped particle bunches is a minimum. We do this first for the case of a wave with an amplitude growing slowly in time, which is a much simpler problem. We then point out the differences in the actual case of spatially-varying amplitude.

We suppose that initially the amplitude of the wave vanishes, and there is a monoenergetic beam with momentum $p_i = 1 + \Delta p$, where 1 is the phase velocity of the wave in our dimensionless units. The phase space corresponding to this situation is shown in Fig. 8a, which also gives the areas of the relevant phase-space regions. The value of the adiabatic invariant associated with the particles in this beam is the familiar action: $I_i = (1/2\pi) \oint p dq = p_i$. As the wave amplitude grows, the phase space contour on which these particles lie becomes distorted but always has below it the same area.

There eventually comes a time, which we call the trapping time t_x, when the area under the upper branch of the separatrix equals the phase-space area under the initial ensemble of particles. At the trapping time, the value of the action on the separatrix

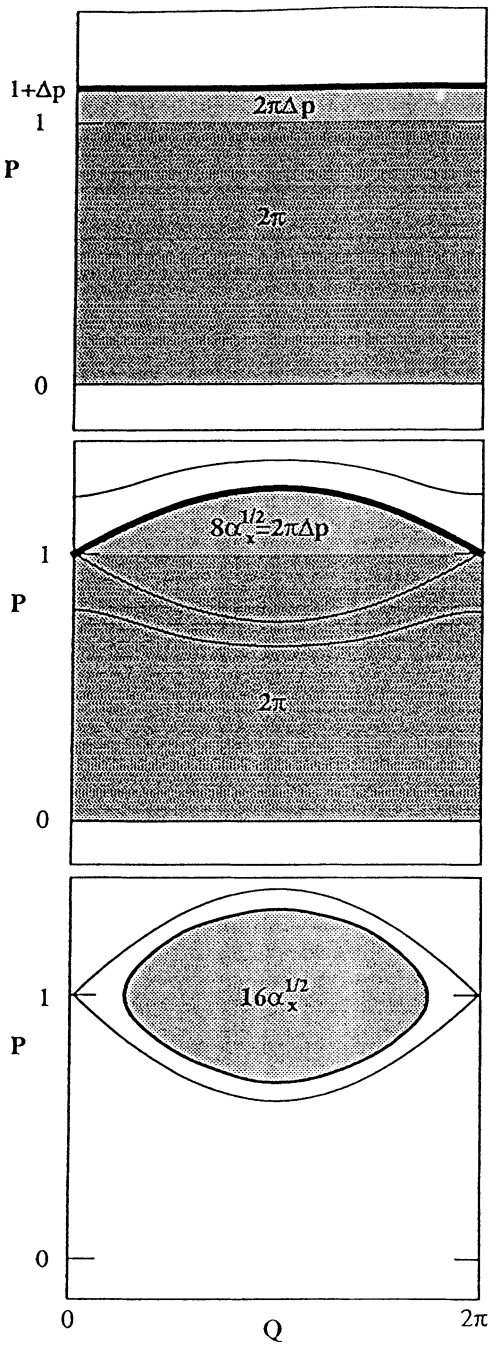

FIGURE 8: Evolution of the trapping process for the case of a wave with an amplitude growing slowly in time. The heavy line indicates schematically the location of the particles.

— given in general by $Y(\varepsilon t) = 1 + (4/\pi)\alpha^{1/2}(\varepsilon t)$ — is equal to I_i. This situation is shown schematically in Fig. 8b. Beyond this time, there does not exist a contour in the phase-space region of passing particles with a corresponding action equal to I_i. Thus the particles must become trapped.

As the wave amplitude increases further, these trapped particles remain on a phase-space contour enclosing an area $16\alpha_x^{1/2} = 4\pi\Delta p$, where $\alpha_x \equiv (\varepsilon t_x)$, since that is the area enclosed by the separatrix at the time of trapping. In other words, the final value of the action for these particles is $I_f = (1/2\pi) \oint p dq = (8/\pi)\alpha_x^{1/2}$. This situation is shown schematically in Fig. 8c.

We now know how to determine the phase-space area (i.e., the longitudinal emittance) associated with an adiabatically trapped bunch of particles, for the case of a wave with time-varying amplitude. An initial beam of particles with momenta spread between $p = 1$ and $p = 1 + \Delta p$ occupies a phase-space area (per wavelength) of $2\pi\Delta p$. As the wave amplitude increases from zero, first the particles with $p = 1$ become trapped. As the amplitude continues to grow, the larger momentum particles become trapped. The largest momentum particles become trapped at an amplitude α_x satisfying $2\pi\Delta p = 8\alpha_x^{1/2}$. After trapping, these particles are spread throughout a region of area $16\alpha_x^{1/2}$. It seems that phase-space area has grown. In fact, only half of this area is populated; however, phase mixing due to the dependence of the bounce or synchrotron frequency on energy leads ultimately to the spreading of particles throughout the entire area in a coarse-grained sense. This emittance increase is just a consequence of poor matching between the beam and the accelerating potential of the RFQ.

If, instead, the initial beam extends from $p = 1-\Delta p$ to $p = 1+\Delta p$, then the particles of greatest and least momentum trap at the same time, and there is no apparent increase of area. Such a beam is correctly matched to the RFQ, because the final longitudinal emittance, being equal to the initial emittance is as small as possible, given Liouville's theorem.

Now we consider the actual case of a wave with amplitude that increases slowly in space. Just as in the time-varying case, we minimize the longitudinal emittance of each trapped-particle bunch by requiring that the particles of greatest and least momentum trap at the same wave amplitude. We suppose that the particles in the initial beam are spread in momentum between a lower bound p_i and an upper bound p_f. Using the ideas of Section 4, we readily find that the above requirement is satisfied if p_i and p_f are related to each other by Eq. (13). The function on the right hand side of Eq. (13) is its own inverse, so p_i and p_f can be interchanged with each other.

To illustrate how this result differs from that of the time-varying case, we suppose that $p_f = 1 + \Delta p$ and that $\Delta p \ll 1$. Expanding Eq. (13) in this limit yields

$$p_i = 1 - \Delta p + \left(\frac{\pi^2}{8} - 1\right)\Delta p^2 + \mathbf{O}(\Delta p^3)\,. \tag{22}$$

Thus p_i differs from the value predicted by the analysis of the time-varying case, $1-\Delta p$, by only a small amount when the relative momentum spread of the initial beam is small. This difference increases as the initial beam is made warmer. For example, the warmest beam that could be completely trapped by a spatially-varying wave, without

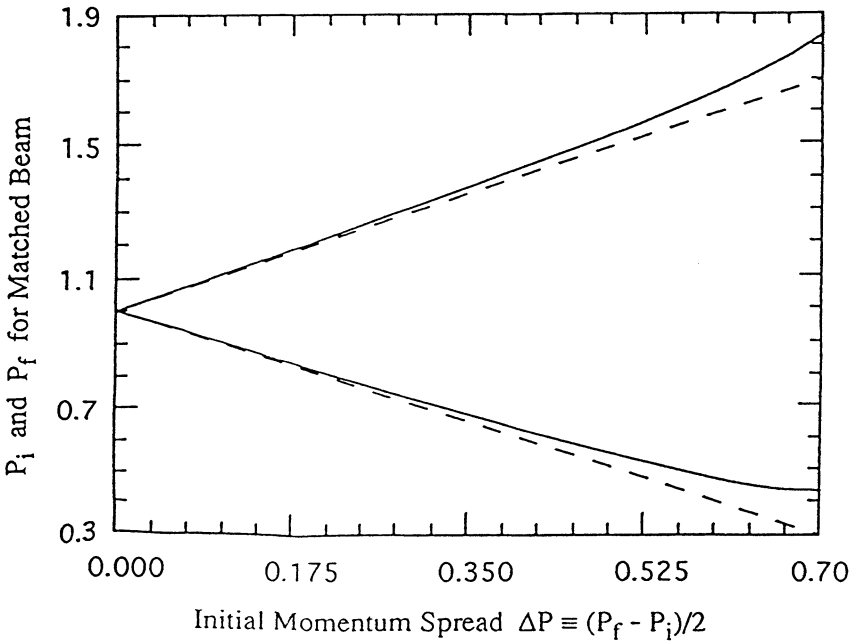

FIGURE 9: The minimum (p_i) and maximum (p_f) longitudinal momenta of a continuous beam, as a function of the initial momentum spread, required for minimum emittance growth during adiabatic trapping. The solid lines are the result for a spatially-varying wave, while the dashed lines are for a time-varying wave. The lower curves correspond to p_i and the upper curves to p_f.

any of the particles being reflected, would have the upper-momentum bound given by $p_a \approx 1.853$ of Eq. (16a) and the lower-momentum bound given by $p_b \approx 0.435$ of Eq. (16b); these two values are not at all symmetric about the phase velocity $p = 1$.

Figure 9 presents these ideas graphically. Assuming an initial beam with total longitudinal momentum spread of $2\Delta p$, the dashed lines in Fig. 9 show the values of p_i and p_f that one would choose in order to longitudinally match a beam into a *time*-varying wave: $p_i(\Delta p) = 1-\Delta p$, and $p_f(\Delta p) = 1+\Delta p$. The solid lines in Fig. 9 show the corresponding values of Δp for the case of a *spatially* varying wave. As noted above, the two predictions agree for small Δp and diverge significantly as Δp becomes of order unity. For larger values of Δp than those shown in Fig. 9, the lowest-momentum particles would be ponderomotively reflected, while some of the highest-momentum particles would be resonantly reflected — two physical phenomena not present in the *time*-varying system.

7.2 Compton Regime FEL with a Recirculating Electron Beam

Short wavelength FEL's operate in the single-particle or Compton regime. Because these devices cannot efficiently extract energy from an electron beam during a single

pass, a recirculation scheme is desirable. For example, one could accelerate the beam after each pass through the FEL, then reinject it once the extracted energy had been restored.

Because the FEL interaction is a resonant process, the injected electrons must all have an energy close to the resonant energy in order for lasing to occur. Unfortunately, nonadiabatic effects during trapping and detrapping significantly heat the beam during each pass through the FEL. This heating would severely limit the number of times a single beam could be recirculated.

However, if the electron beam is trapped and detrapped adiabatically, and it is appropriately matched to the wave potential, then there is no increase in the longitudinal emittance (i.e., no heating) to lowest order in the adiabatic parameter ε. This issue was addressed in detail in our discussion above regarding the trapping of ions in an RFQ. To achieve adiabatic trapping and detrapping, the FEL wiggler magnet would have to have tapered trapping and detrapping sections, in order to ramp the magnetic field up and then down. Thus, the required structure would be approximately three times as long as a standard tapered wiggler.

We now briefly consider a model Hamiltonian describing the longitudinal dynamics of an electron in an FEL in order to point out the similarities with our model. The relativistic Hamiltonian for a particle in a magnetic field has the form $H = [1 + (\mathbf{P} - \mathbf{A})^2]^{1/2}$, where $\mathbf{A}$ is the vector potential, $\mathbf{P} = \mathbf{p} + \mathbf{A}$ is the canonical momentum, and $\mathbf{p} = \gamma m \mathbf{v}$ is the usual relativistic momentum. We have normalized units such that m, c and e are all unity.

We will neglect any variation of the magnetic field along the transverse directions. If we assume both the wiggler field and the laser field are circularly polarized, this implies vector potentials of the form

$$\mathbf{A}_w = -A_w(z)\left[\hat{\mathbf{x}}\cos\left(\int_0^z k_w(z')dz'\right) + \hat{\mathbf{y}}\sin\left(\int_0^z k_w(z')dz'\right)\right], \tag{23a}$$

$$\mathbf{A}_r = A_r(z)\left[\hat{\mathbf{x}}\cos\left(\int_0^z k_r(z')dz' - \omega_r t\right) + \hat{\mathbf{y}}\sin\left(\int_0^z k_r(z')dz' - \omega_r t\right)\right]. \tag{23b}$$

The w subscript refers to the wiggler, the r subscript refers to the radiation field, z is the longitudinal coordinate, and the full vector potential is $\mathbf{A} = \mathbf{A}_w + \mathbf{A}_r$.

Because H is independent of the transverse coordinates, the transverse canonical momenta P_x and P_y are constants of the motion. For the sake of simplicity, we assume these constants to be zero here. Because there is no z component of the vector potential, the canonical momentum P_z is equal to the longitudinal relativistic momentum p_z.

Combining these various results yields the following Hamiltonian:

$$H(z,p_z,t) =$$

$$= \sqrt{1+p_z^2+A_w^2(z)+A_r^2(z)+2A_w(z)A_r(z)\cos\left(\int_0^z [k_w(z')+k_r(z')]dz' - \omega_r t\right)} \quad (24$$

The cosine term inside the radical is known as the ponderomotive potential; it is the traveling wave in which the electrons trap, are decelerated, then subsequently detrap. The methods developed in this paper could be directly applied to the above Hamiltonian.

In fact, the ideas presented here have motivated a proposed experiment[23] to build and test a prototype wiggler magnet with adiabatic ramping of the magnetic field, which would be very advantageous, for example, for use in a storage-ring FEL.

7.3 Plasma Beat-Wave Acceleration

Bertrand *et al.*[3] have modeled the phenomenon of PBWA, in which a Langmuir wave (a longitudinal electrostatic plasma wave) is driven by two incident electromagnetic waves with frequencies that differ by the electron plasma frequency. The evolution of the longitudinal electric field is rather complicated, but it exhibits two important features. First, the field is very coherent throughout every stage of its evolution. In other words, it can be approximately described by a sinusoidal function (traveling at the phase velocity) multiplied by an envelope function. Second, this envelope function varies slowly in time and position.

The motion of a test particle in the longitudinal electric field can be described by the following Hamiltonian [see Eq. (20) of Ref. 3]:

$$H(z,p_z,t) = \sqrt{m^2c^4+p_z^2c^2} - e\Phi_0\left(\frac{z}{L},\frac{t}{T}\right)\sin^2\left[\frac{1}{2}k(z-v_{ph}t-z_0)\right]. \quad (25a)$$

Here z is the longitudinal position, p_z the relativistic momentum, t the time, m the electron mass, c the speed of light, $-e$ the electron charge, Φ_0 the envelope of the electric potential, L the length scale for changes in Φ_0, T the time scale for changes in Φ_0, k the wave number of the wave, ω the frequency of the wave, $v_{ph} = \omega/k$ the phase velocity of the wave, and z_0 a constant phase factor. If we choose units such that m, c, and k are all unity, then we obtain the dimensionless Hamiltonian

$$H(z,p_z,t) = \sqrt{1+p_z^2} - \alpha(\varepsilon_z z,\varepsilon_t t)\sin^2\left[\frac{1}{2}(z-\beta_{ph}t-z_0)\right], \quad (25b)$$

where $\alpha \equiv -e\Phi_0/mc^2$, $\varepsilon_z \equiv 1/kL$, $\varepsilon_t \equiv 1/kcT$ and $\beta_{ph} \equiv v_{ph}/c$.

This Hamiltonian is very similar to the wavepacket Hamiltonian of Eq. (2). The important differences are that it is relativistic, the amplitude envelope depends slowly

on time as well as position, and there is an additional dimensionless parameter β_{ph}. For the simulations presented in Ref. 3, $\varepsilon \approx \varepsilon_t \approx 0.02$, $\beta_{ph} \approx 0.88$, and the maximum amplitude of the wave envelope is $\alpha_0 \approx 0.29$.

The analytic techniques developed in this paper represent a good starting point for solving more complicated systems such as the Hamiltonian of Eq. (25), because the wave parameters are varying slowly and the dimensionless wave amplitude is a significant fraction of unity. The lower box in Fig. 6c of Ref. 3 shows part of the electron fluid detrapping from the plasma wave with momentum greater than the resonant momentum of the wave. This fluid consists of electrons that were trapped out of the (low momentum) thermal distribution, then subsequently detrapped with significantly larger momentum.

Of greater relevance to our work, which deals with test particles rather than fluid motion, are the electrons which would be accelerated by such a plasma wave. The goal in plasma beat-wave acceleration is to inject the electrons at a momentum (energy) below the resonant momentum of the plasma wave, such that they are all trapped, then to have the electrons detrap further down the device, with a momentum above the resonant value. The energy of the electrons can be increased significantly in this way. In other work,[4] extensive 1-D, 2-D, and 3-D numerical simulations were conducted to examine the test-particle dynamics of electrons injected into a PBWA.

In Ref. 4, however, the wave was assumed to be of constant amplitude. However, abrupt trapping and detrapping of the electrons would result in such large longitudinal emittance growth that only a small fraction of them would reach the desired energy. Instead, one must have a wave that rises and falls adiabatically along the length of the PWBA, as does the wave seen in the numerical simulations presented in Fig. 6 of Ref. 3. Then the acceleration process would be analogous to that shown schematically in our Fig. 3; the electrons would be initially following trajectories that correspond to the adiabatic-invariant contour labelled c, then after detrapping would follow trajectories corresponding to the adiabatic-invariant contour labelled b.

In fact, our techniques have recently been applied[13] to a relativistic version of the Hamiltonian in Eq. (2) in order to properly treat electron dynamics in a PBWA in the adiabatic limit. It was shown in that work that correctly treating the plasma wave as a spatially-varying structure (rather than time-varying or constant-amplitude) resulted in significantly different predictions for the electron dynamics.

8 CONCLUSIONS

We have shown in this paper how to correctly apply adiabatic theory to the problem of charged particles interacting with a simple spatially-varying wave structure of arbitrarily-large amplitude, in the limit that the bounce time of trapped particles is short compared with the transit time of a resonant particle moving through the wave. We found that the adiabatic invariant is not equal, even in lowest order, to the action, which is the familiar invariant from the time-varying case. The general ideas developed here can be straightforwardly applied to more complicated spatially-varying systems.

We showed that contour plots of the adiabatic invariant provide an understand-

ing of the underlying structure of the particle dynamics, without having to solve any differential equations or numerically integrate any equations of motion. The topology of the adiabatic-invariant contours is quite rich, and this topology changes dramatically as the maximum wave amplitude A_0 increases through the critical value $A_{T1} = (4/\pi^2)(m\omega^2/k^2e)$, then again as it increases through the critical value $A_{T2} \approx 0.636(m\omega^2/k^2e)$. Using the lowest-order dynamical picture provided by adiabatic theory, we correctly predicted the basic features of the wave-particle interaction as observed in the previous numerical work of Fuchs, Krapchev, Ram, and Bers.[11]

In the limit of small wave amplitude, our analysis overlaps with that of nonrelativistic ponderomotive theory. We have shown that these two theories agree in this limit in their prediction of the range of initial momenta (when far from the wave) that result in the ponderomotive reflection of particles. As the maximum wave amplitude is increased, the range of momenta predicted by adiabatic theory falls slightly below that predicted by ponderomotive theory, and finally saturates for $A_0 \geq A_{T2}$. Numerical simulations have verified the adiabatic prediction. This is the first result of which we are aware that treats ponderomotive reflection for arbitrarily large wave amplitudes.

The model Hamiltonian that we treat here, given in Eqs. (1) and (2), is relevant to the longitudinal beam dynamics of ions in an RFQ. In particular, we explain how to correctly match an ion beam to an RFQ (neglecting transverse motion) so as to minimize growth of the longitudinal emittance during trapping. Our model is also relevant to the longitudinal dynamics of electrons in an FEL or a plasma beat-wave accelerator. In order for the trapping and detrapping of electrons in an FEL to be adiabatic, the wiggler magnet must have appropriately tapered trapping and detrapping sections — our results suggest that such a wiggler would be useful for a Compton-regime FEL with a recirculating electron beam.

ACKNOWLEDGMENTS

We would like to thank Tasso Kaper for his comments on early versions of this manuscript. This work was supported by the U.S. Department of Energy under contract no. DE-FG02-86ER40302 and by Independent Research and Development funds of the Grumman Aerospace Corporation.

APPENDIX A

Finding the adiabatic-invariant contour with an x point:

We explain here how to numerically find the value of the adiabatic invariant on the one adiabatic-invariant contour with an x point. We call this value J_{xb}, because it corresponds to trajectories in phase-space region b. In the small- and intermediate-amplitude regimes, the x point contour is the ponderomotive contour and $J_{xb} = J_{\text{pond}}$.

In order for a contour of constant $J(\bar{p}_\phi, \lambda \equiv \varepsilon q)$ to have an x-point, certain criteria must be satisfied. First of all, the partial derivatives of J with respect to $\bar{p}_\phi$ and λ must

both vanish at the same point. In addition, because an x point is a saddle point, the second-derivative test of differential calculus (see, e.g., Ref. 24) must be satisfied at this point. We evaluate all of the first and second derivatives of $J_P(\bar{p}_\phi, \lambda)$ in region b and consider whether or not the above criteria can be satisfied. The same criteria could be applied to J_P in region a, as well as to J_T, and one would find that none of the corresponding contours can have an x point.

The function $J_P(\bar{p}_\phi, \lambda)$, as determined by Eqs. (8a) and (9a), depends on the function $E_\phi(\bar{p}_\phi, \lambda)$, which is implicitly defined as the inversion of Eq. (9a). We need to evaluate the partial derivatives of $J_P(\bar{p}_\phi, \lambda)$ with respect to $\bar{p}_\phi$ and λ in order to determine whether or not they vanish at the same point. Before doing this, we must learn how to differentiate the implicit function E_ϕ.

If we differentiate both sides of the equation $\bar{p}_\phi \equiv \bar{p}_\phi(E_\phi(\bar{p}_\phi, \lambda), \lambda)$ with respect to $\bar{p}_\phi$ and λ, treating $\bar{p}_\phi$ and λ as independent variables, we obtain

$$\frac{\partial E_\phi}{\partial \bar{p}_\phi}(\bar{p}_\phi, \lambda) \equiv \left\{ \frac{\partial \bar{p}_\phi}{\partial E_\phi}[E_\phi(\bar{p}_\phi, \lambda), \lambda] \right\}^{-1}, \tag{A1a}$$

$$\frac{\partial E_\phi}{\partial \lambda}(\bar{p}_\phi, \lambda) \equiv -\left\{ \frac{\partial \bar{p}_\phi}{\partial E_\phi}[E_\phi(\bar{p}_\phi, \lambda), \lambda] \right\}^{-1} \frac{\partial \bar{p}_\phi}{\partial \lambda}[E_\phi(\bar{p}_\phi, \lambda), \lambda]. \tag{A1b}$$

In order to use Eqs. (A1a) and (A1b), we must know the partial derivatives of $\bar{p}_\phi(E_\phi, \lambda)$ in region b, which can be obtained by straightforward differentiation of Eq. (9a):

$$\frac{\partial \bar{p}_\phi}{\partial E_\phi}(E_\phi, \lambda) = -\frac{\sqrt{2}}{\pi}[E_\phi + \alpha(\lambda)]^{-1/2}\mathbf{K}(k), \tag{A2a}$$

$$\frac{\partial \bar{p}_\phi}{\partial \lambda}(E_\phi, \lambda) = -\frac{\sqrt{2}}{\pi}\frac{\alpha'(\lambda)}{\alpha(\lambda)}[E_\phi + \alpha(\lambda)]^{-1/2}\{E_\phi \mathbf{E}(k) - [E_\phi - \alpha(\lambda)]\mathbf{K}(k)\}, \tag{A2b}$$

where α' is the derivative of α with respect to λ, and the function $k(E_\phi, \lambda)$ is defined below Eq. (9b).

Using the chain rule and the results above, we obtain the partial derivatives of J_P:

$$\frac{\partial J_P}{\partial \bar{p}_\phi}(\bar{p}_\phi, \lambda) = 1 - \frac{\pi}{\sqrt{2}}\frac{[E_\phi + \alpha(\lambda)]^{1/2}}{\mathbf{K}(k)}. \tag{A3a}$$

$$\frac{\partial J_P}{\partial \lambda}(\bar{p}_\phi, \lambda) = \frac{\alpha'}{\alpha}\left\{ [E_\phi - \alpha(\lambda)] - E_\phi \frac{\mathbf{E}(k)}{\mathbf{K}(k)} \right\}. \tag{A3b}$$

The requirement $\partial J_P/\partial \lambda = 0$ can be trivially satisfied by choosing $\lambda = 0$, for which $\alpha' = 0$ (because the maximum value of α occurs, by assumption, at $\lambda \equiv \varepsilon_q = 0$).

It is not obvious under what conditions this requirement can be satisfied for $\lambda \neq 0$; however, the only x point does lie on the line $\lambda = 0$, and we will use this fact to simplify further analysis. Consideration of the requirement $\partial J_P/\partial \bar{p}_\phi = 0$ is somewhat more involved.

We can show that $\partial J_P/\partial \bar{p}_\phi$ vanishes at least once on the line $\lambda = 0$, for any finite value of α_0, by showing that it changes sign from positive to negative as $\bar{p}_\phi$ is decreased from its value on the lower lip, $-(4/\pi)\alpha_0^{1/2}$, towards $-\infty$. Because $E_\phi \to \alpha_0$ as $\bar{p}_\phi \to -(4/\pi)\alpha_0^{1/2}$ (for $\lambda = 0$) in region b, we can find a value of E_ϕ such that $(E_\phi - \alpha_0)/\alpha_0 \ll 1$ for any finite value of α_0. In this limit, Eq. (A3a) becomes

$$\frac{\partial J_P}{\partial \bar{p}_\phi} = 1 - \frac{2\pi\alpha_0^{1/2}}{\ln|32\alpha_0/(E_\phi - \alpha_0)|}\{1 + \mathbf{O}[(E_\phi - \alpha_0)/\alpha_0]\} . \tag{A4a}$$

For a small enough value of $(E_\phi - \alpha_0)$, the right hand side of (A4a) will be positive. Furthermore, because $E_\phi \to \infty$ as $\bar{p}_\phi \to -\infty$ in region b, we can find a value of E_ϕ such that $\alpha_0/E_\phi \ll 1$ for any finite value of α_0. In this limit, Eq. (A3a) becomes

$$\frac{\partial J_P}{\partial \bar{p}_\phi} = 1 - (2E_\phi)^{1/2}\left[1 - \frac{9}{16}(\alpha_0/E_\phi)^2 + \mathbf{O}(\alpha_0/E_\phi)^3\right] . \tag{A4b}$$

For a large enough value of E_ϕ, the right hand side of (A4b) will be negative. Therefore, there is at least one point along the line $\lambda = 0$ where both partial derivatives of J_P vanish. [We keep the $\mathbf{O}(\alpha_0/E_\phi)^2$ term explicitly in Eq. (A4b) because it will be useful in App. D.]

According to the second-derivative test, the point where both partial derivatives vanish is a saddle point if the function $D_2(\bar{p}_\phi, \lambda)$ is negative at that point. This function is defined as

$$D_2(\bar{p}_\phi, \lambda) \equiv \frac{\partial^2 J_P}{\partial \bar{p}_\phi^2}(\bar{p}_\phi, \lambda)\frac{\partial^2 J_P}{\partial \lambda^2}(\bar{p}_\phi, \lambda) - \left[\frac{\partial^2 J_P}{\partial \bar{p}_\phi \partial \lambda}(\bar{p}_\phi, \lambda)\right]^2 . \tag{A5}$$

We are interested in the value of $D_2(\bar{p}_\phi, \lambda)$ for $\lambda = 0$ and for $\bar{p}_\phi$ such that $\partial J_{0b}/\partial \bar{p}_\phi(\bar{p}_\phi, 0) = 0$.

Further differentiating Eqs. (A3) yields:

$$\frac{\partial^2 J_P}{\partial \bar{p}_\phi^2}(\bar{p}_\phi, \lambda = 0) = \frac{\pi^2}{4}\frac{E_\phi + \alpha_0}{E_\phi - \alpha_0}\frac{\mathbf{E}(k)}{\mathbf{K}^3(k)} , \tag{A6a}$$

$$\frac{\partial^2 J_P}{\partial \lambda^2}(\bar{p}_\phi, \lambda = 0) = \frac{\alpha''}{\alpha_0}\left[(E_\phi - \alpha_0) - E_\phi\frac{\mathbf{E}(k)}{\mathbf{K}(k)}\right] , \tag{A6b}$$

$$\frac{\partial^2 J_P}{\partial \bar{p}_\phi, \partial \lambda}(\bar{p}_\phi, \lambda = 0) = 0 , \tag{A6c}$$

where α'' is the second derivative of α with respect to λ. The right-hand side of Eq. (A6a) is a positive definite quantity. The mixed partial derivative of J_P vanishes

identically at $\lambda = 0$, because it is proportional to α'. Thus, any point where both first derivatives vanish is an x-point if $\partial^2 J_P/\partial\lambda^2 < 0$ at that point. We have found that, for any value of α_0, the equation $\partial J_P/\partial\bar{p}_\phi = 0$ can be satisfied for one and only one value of E_ϕ and that this point is in each case an x-point.

APPENDIX B

Finding α_{T1}, the transition between the small- and intermediate-amplitude regimes.

As the maximum wave amplitude α_0 increases through the critical value $\alpha_{T1} \equiv 4/\pi^2$, the topology of the adiabatic-invariant contour plot changes from that of the small-amplitude regime shown in Fig. 3 to that of the intermediate-amplitude regime shown in Fig. 4. We determine the value of α_{T1} by considering the critical contour labeled $p_{\min}$ in Fig. 3. This contour grazes the lower lip, so the adiabatic invariant associated with it is $J_{\min} = Y_b(\alpha_0)$. Trajectories corresponding to this contour have momentum $p_{\min}$ when far from the wave, so we also have $J_{\min} = j(p_{\min})$.

These two functions and their derivatives have the following form:

$$Y_b(\alpha_0) = \alpha_0 - \frac{4}{\pi}\alpha_0^{1/2}; \quad j(p_{\min}) = \frac{1}{2}(p_{\min}^2 - 1); \tag{B1}$$

$$Y_b'(\alpha_0) = 1 - \frac{2}{\pi}\alpha_0^{-1/2}; \quad j'(p_{\min}) = p_{\min}; \tag{B2}$$

$$Y_b''(\alpha_0) = \frac{1}{\pi}\alpha_0^{-3/2}; \qquad j''(p_{\min}) = 1. \tag{B3}$$

As α_0 increases from zero, Y_b decreases from zero and reaches its minimum value of $-4/\pi^2$ when $\alpha_0 = 4/\pi^2$, then begins increasing towards zero. The value of $p_{\min}$ corresponding to $\alpha_0 = 0$ is $p_{\min} = 1$, and $p_{\min}$ decreases towards zero as α_0 increases. As this occurs, j decreases from zero very much as Y_b does.

Thus we have a one-to-one correspondence between $Y_b(\alpha_0)$ and $j(p_{\min})$ for $\alpha_0 \leq 4/\pi^2$, and the $J_{\min}$ contour exists as shown in Fig. 3. The value of $p_{\min}$ corresponding to $\alpha_0 = 4/\pi^2$ is $p_{\min} = (1 - 8/\pi^2)^{1/2} \equiv p_b$, for which $j = -4/\pi^2$. However, $j(p_{\min})$ becomes even more negative as $p_{\min}$ approaches zero, where it reaches its minimum value $j(0) = -1/2$.

Therefore, the $J_{\min}$ contour as drawn in Fig. 3 cannot exist for α_0 slightly larger than $4/\pi^2$. For $\alpha_0 > 4/\pi^2$, the contour with $J_P = J_{Pb} \equiv -4/\pi^2$ must still touch the lower lip where $\alpha(\varepsilon q) = 4/\pi^2$, while contours with J_P slightly more negative than J_{Pb} (i.e., p_i slightly less than p_b) must not touch the lower lip at all. Continuity thus requires that the critical J_{Pb} contour graze the lower lip where $\alpha = 4/\pi^2$ and lie below the lower lip where $\alpha > 4/\pi^2$. Continuity also requires that there be other contours, with values of J_P between J_{Pb} and $Y_b(\alpha_0)$, that lie between the J_{Pb} contour and the bottom of the lower lip.

This topology is in fact what is observed in Fig. 4. Thus, the critical value of α_0 separating the small-amplitude and intermediate-amplitude regimes is $\alpha_{T1} \equiv 4/\pi^2$.

APPENDIX C

Details of the large-amplitude regime.

For $\alpha_0 > \alpha_{T2}$, the ponderomotive contour is split in two by the lower lip and no longer has an x point (see Fig. 5). However, as we have stated above in Appendix A, there persists a contour with an x-point below the lower lip. This critical contour, which we call the J_{xb} contour, is shown schematically in Fig. C1: in addition to having an x-point, it intersects the lower lip in two points. We denote the wave amplitude at these points of intersection by α_{xb}. Just below the $p_{\max}$ contour in region a, there is another critical contour, also shown schematically in Fig. C1, which we call the J_{xa} contour.

Of those trajectories corresponding to contours in between the $J_{\max}$ and J_{xa} contours, some trap in the wave and then detrap back into region a, while others cross the separatrix into region b, remain briefly in this region (the corresponding adiabatic invariant contours lie between the lower lip and the x-point of the J_{xb} contour), then cross the separatrix back into region a. The topology of these contours is analogous to that of the contours in Fig. 4 lying between the critical contours p_a and $p_{\max}$.

These details regarding the topology of the large-amplitude regime were not shown in Fig. 5, because they affect only a very small class of trajectories. We can justify this assertion in two ways. First, we show that the differences $J_{\max} - J_{xa}$ and $J_{\min} - J_{xb}$ vanish exponentially fast as α_0 increases beyond α_{T2}. [We define $J_{\min} \equiv Y_b(\alpha_0)$, $J_{\max} \equiv Y_a(\alpha_0)$, $J_{xb} \equiv Y_b(\alpha_{xb})$, and $J_{xa} \equiv Y_a(\alpha_{xb})$.] Second, we show that α_{xb}, the wave amplitude at which the J_{xb} contour intersects the lower lip, differs from α_0 by an amount that also vanishes exponentially fast as α_0 increases.

When numerically solving for α_{T2}, we also found that $(E_\phi - \alpha_0) \approx 0.126$ at the x-point. Therefore $(E_\phi - \alpha_0)/\alpha_0 \approx 0.198$ is small for $\alpha_0 \geq \alpha_{T2}$. If we expand J_P in this limit, we find that

$$J_P(E_\phi, 0) = E_\phi - \frac{4}{\pi}\alpha_0^{1/2}\left[1 + \frac{E_\phi - \alpha_0}{8\alpha_0}\left(\ln\left|\frac{32\alpha_0}{E_\phi - \alpha_0}\right| + 1\right)\right] + \mathbf{O}\{(E_\phi - \alpha_0)/\alpha_0]^2\}\,. \tag{C1}$$

Furthermore, the expansion of $\partial J_P/\partial \bar{p}_\phi$ in this limit is given by Eq. (A4a). If we demand that $\partial J_P/\partial \bar{p}_\phi$ vanish, then we find the approximate value of $E_\phi - \alpha_0$ at the x point:

$$E_\phi - \alpha_0 = 32\alpha_0 \exp(-2\pi\alpha_0^{1/2})\,\{1 + \mathbf{O}[(E_\phi - \alpha_0)/\alpha_0]\}. \tag{C2}$$

From Eq. (C2), we see that the ratio $(E_\phi - \alpha_0)/\alpha_0$ gets rapidly smaller as α_0 increases. Plugging Eq. (C2) into Eq. (C1) yields J_{xb}:

$$J_{xb} = \alpha_0 - \frac{4}{\pi}\alpha_0^{1/2}[1 + \exp(-2\pi\alpha_0^{1/2})] + \mathbf{O}[\exp(-4\pi\alpha_0^{1/2})]\,. \tag{C3}$$

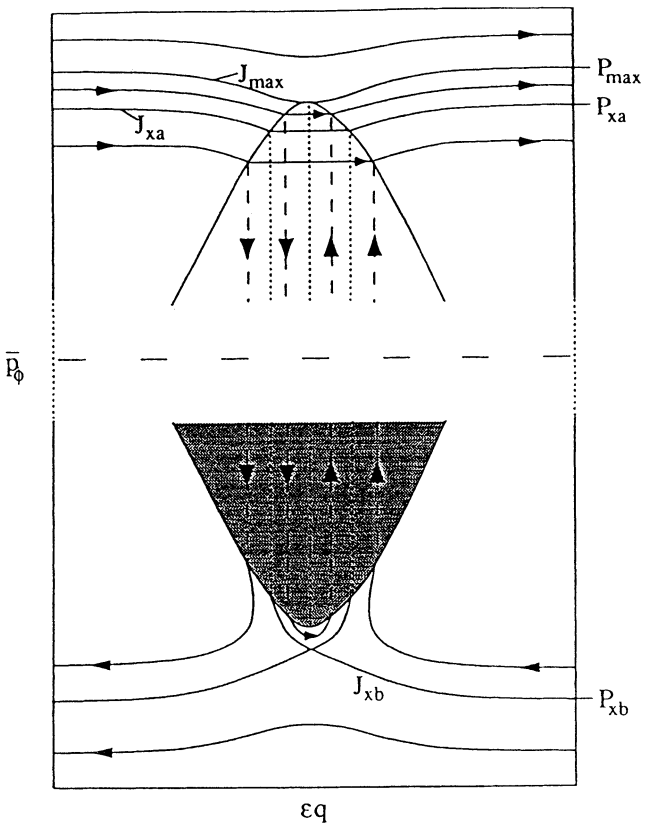

FIGURE C1: This figure is a schematic presentation of certain details regarding action contours in the $\bar{p}_\phi - \varepsilon q$ plane, for α_0 in the large-amplitude regime. Two new critical contours, labeled J_{xa} and J_{xb}, are shown. In addition, it is shown that there exists a class of contours between the x-point of the J_{xb} contour and the bottom of the lower lip.

Now we can use Eq. (C3) to find α_{xb}, the value of α_x at which the J_{xb} contour intersects the lower lip, by letting $Y_b = J_{xb}$ and using Eq. (10b) to solve for α_x. Having done this, one finds

$$J_{\min} - J_{xb} = J_{\max} - J_{xa} = \frac{16}{\pi}\alpha_0^{1/2}\exp(-2\pi\alpha_0^{1/2}) + \mathbf{O}[\exp(-4\pi\alpha_0^{1/2})]\,, \tag{C4a}$$

$$\alpha_0 - \alpha_{xb} = \frac{16}{\pi}\,\frac{\alpha_0\exp(-2\pi\alpha_0^{1/2})}{\alpha_0^{1/2} - 2/\pi} + \mathbf{O}[\exp(-4\pi\alpha_0^{1/2})]\,. \tag{C4b}$$

For $\alpha_0 = 2.5$, as is the case in Fig. 5, the right-hand side of Eq. (C4a) is approximately 3.9×10^{-4}, and the right-hand side of Eq. (C4b) is approximately 6.5×10^{-4}. Thus,

given the thickness of the lines used to plot the contours in Fig. 5, we see that the $J_{\max}$ and J_{xa} contours would essentially overlap, and the J_{xb} contour would be indistinguishable from the artificial $J_{\min}$ contour.

APPENDIX D

Finding the ponderomotive contour analytically in the limit of small wave amplitude.

We find $J_{xb} = J_{\text{pond}}$ analytically in the limit of small α_0 in order to compare with ponderomotive theory, which requires a small-amplitude expansion. If we expand J_P in the limit $\alpha_0/E_\phi \ll 1$, we obtain

$$J_P(E_\phi, 0) = E_\phi - \sqrt{2E_\phi}\left[1 - \frac{1}{16}(\alpha_0/E_\phi)^2 + \mathbf{O}(\alpha_0/E_\phi)^3\right]. \tag{D1}$$

Furthermore, $\partial J_P/\partial \bar{p}_\phi$ is given in this limit by Eq. (A4b). Requiring $\partial J_P/\partial \bar{p}_\phi = 0$ yields the value of E_ϕ at the x-point in this limit:

$$E_\phi = \frac{1}{2} + \frac{9}{4}\alpha_0^2 + \mathbf{O}(\alpha_0)^3. \tag{D2}$$

If we now insert Eq. (D2) into Eq. (D1), we obtain J_{pond} in the limit of small α_0:

$$J_{\text{pond}} = -\frac{1}{2} + \frac{1}{4}\alpha_0^2 + \mathbf{O}(\alpha_0)^3. \tag{D3}$$

Finally, we can use this result in Eq. (15) to obtain p_{pond} in the limit of small α_0:

$$p_{\text{pond}} = 2^{-1/2}\alpha_0[1 + \mathbf{O}(\alpha_0)]. \tag{D4}$$

Comparison of Eq. (D4) with Eq. (19) shows that adiabatic theory agrees with ponderomotive theory in the limit of small α_0, which indeed it must.

REFERENCES

1. I. M. Kapchinskii and F. A. Teplyakov, Prib. Tekh. Eksp. **No. 2**, 19 (1970) [Instrum. Exp. Tech. (USSR) **No. 2**, 322 (1970)].
2. C. W. Roberson and P. Sprangle, Phys. Fluids B **1**, 3 (1989).
3. P. Bertrand, A. Ghizzo, T. W. Johnston, M. Shoucri, E. Fijalkow, and M. R. Feix, Phys. Fluids B **2**, 1028 (1990).
4. R. L. Williams, C. E. Clayton, C. Joshi, T. Katsouleas, and W. B. Mori, Laser Part. Beams **8**, 427 (1990).
5. M. Kruskal, J. Math. Phys. **3**, 806 (1962).
6. C. S. Gardner, Phys. Rev. **115**, 791 (1959); R. G. Littlejohn, J. Plasma Phys. **29**, 11 (1983).
7. R. W. B. Best, Physica **40**, 182 (1968).
8. R. T. Skodje and J. R. Cary, Comp. Phys. Rep. **8**, 221 (1988).
9. D. L. Bruhwiler and J. R. Cary, Phys. Rev. Lett. **68**, 255 (1992).
10. D. L. Bruhwiler, Ph.D. thesis, University of Colorado at Boulder (1990).

11. V. Fuchs, V. Krapchev, A. Ram, and A. Bers, Physica D **14**, 141 (1985).
12. J. R. Cary and D. L. Bruhwiler, "Adiabatic Invariance for Spatially Dependent Accelerating Structures," in *Nonlinear Dynamics and Particle Acceleration*, eds. Y. H. Ichikawa and T. Tajima, (AIP, New York, 1991), p. 67.
13. P. Mora, "Particle acceleration in a relativistic wave in the adiabatic regime," Phys. Fluids B **4**, 1630 (1992).
14. D. L. Bruhwiler and J. R. Cary, in preparation.
15. R. D. Ruth, "Single-Particle Dynamics in Circular Accelerators," AIP Conference Proceedings, Vol. 153 (1985); A. J. Dragt, "Lectures on Nonlinear Orbit Dynamics," AIP Conference Proceedings, Vol. 87 (1982).
16. I. S. Gradshteyn and I. M. Ryzhik, *Tables of Integrals, Series and Products* (Academic Press, New York, 1980) p. 905.
17. J. R. Cary, D. F. Escande, and J. L. Tennyson, Phys. Rev. A **34**, 4256 (1986).
18. A. I. Neishtadt, Fiz. Plazmy **12**, 992 (1986) [Sov. J. Plasma Phys. **12**, 568 (1986)]; Erratum, Fiz. Plazmy **13**, 765 (1987) [Sov. J. Plasma Phys. **13**, 441 (1987)].
19. J. R. Cary and A. N. Kaufman, Phys. Fluids **24**, 1238 (1981).
20. M. Abramowitz and I. E. Stegun, *Handbook of Mathematical Functions* (National Bureau of Standards, Washington, DC, 1972) p. 416.
21. F. O. Purser, E. A. Wadlinger, O. R. Sander, J. M. Potter, and K. R. Crandall, IEEE Trans. Nucl. Sci. **30**, 3582 (1983).
22. R. H. Stokes, K. R. Crandall, J. E. Stovall, and D. A. Swenson, IEEE Trans. Nucl. Sci. **26**, 3469 (1979); K. R. Crandall, R. H. Stokes, and T. P. Wangler, Proc. 10th Linear Accelerator Conf., Montauk NY, Sep. 10-14, 1979 (Brookhaven National Laboratory, Upton NY, 1980).
23. S. Hendrickson, J. R. Cary, S. Robertson, and S. Makoski, Bull. Am. Phys. Soc. **37**, 1456 (1992); S. Hendrickson, J. R. Cary, and S. Robertson, Bull. Am. Phys. Soc. **38**, 1328 (1993).
24. P. Gillett, *Calculus and Analytic Geometry* (D.C. Heath and Co., Lexington, Mass., 1981), p. 700.